Functional interactomes of the Ebola virus polymerase identified by proximity proteomics in the context of viral replication

Jingru Fang[1,2], Colette Pietzsch[3,4], George Tsaprailis[5], Gogce Crynen[6], Kelvin Frank Cho[7], Alice Y. Ting[8,9], Alexander Bukreyev[3,4,10]*, Juan Carlos de la Torre[2]*, Erica Ollmann Saphire[1]*

[1]La Jolla Institute for Immunology, La Jolla CA 92037

[2]Department of Immunology and Microbiology, Scripps Research, La Jolla CA 92037

[3]Department of Pathology, University of Texas Medical Branch, Galveston, TX 77550

[4]Galveston National Laboratory, University of Texas Medical Branch, Galveston, TX 77550

[5]Proteomics Core, Scripps Research, Jupiter, FL 33458

[6]Bioinformatics and Statistics Core, Scripps Research, Jupiter, FL 33458

[7]Cancer Biology Program, Stanford University, Stanford, CA 94305

[8]Department of Genetics, Department of Biology and Department of Chemistry, Stanford University, Stanford, CA 94305

[9]Chan Zuckerberg Biohub, San Francisco, CA 94158

10 Department of Microbiology and Immunology, University of Texas Medical Branch, Galveston, TX 77550

Correspondence: abukreye@UTMB.EDU, juanct@scripps.edu, erica@lji.org

Lead contact: erica@ji.org

SUMMARY

Ebola virus (EBOV) critically depends on the viral polymerase to replicate and transcribe the viral RNA genome. To examine whether interactions between EBOV polymerase and cellular and viral factors affect distinct viral RNA synthesis events, we applied proximity proteomics to define the cellular interactome of EBOV polymerase, under conditions that recapitulate viral transcription and replication. We engineered EBOV polymerase tagged with the split-biotin ligase split-TurboID, which successfully biotinylated the proximal proteome while retaining polymerase activity. We further analyzed the interactomes in an siRNA-based, functional screen and uncovered 35 host factors, which, when depleted, affect EBOV infection. We validated one host factor, eukaryotic peptide chain release factor subunit 3a (eRF3a/GSPT1), which we show physically and functionally

associates with EBOV polymerase to facilitate viral transcription termination. Our work demonstrates the utility of proximity proteomics to capture the functional host-interactome of the EBOV polymerase and to illuminate host-dependent regulations of viral RNA synthesis.

INTRODUCTION

Ebola virus (EBOV) is a member of the *Filoviridae* family in the order of *Mononegavirales*. Several ebolaviruses cause sporadic outbreaks of hemorrhagic fever disease that are unpredictable in timing and location and are associated with high mortality. The 2013-2016 epidemic emerged far from the location of any previously known EBOV outbreak, entered urban populations, and caused over 11,000 deaths. EBOV re-emerged in 2018 and again in 2020 and 2021 (WHO). Survivors of EBOV infections can experience long-term sequelae (Adekanmbi et al., 2021; Eghrari et al., 2021; Xu et al., 2019), and may harbor virus in immune-privileged sites, posing a risk of transmitting the virus months to years after recovery. Inmazeb, an EBOV-specific monoclonal antibody cocktail, is currently the only FDA-approved treatment for people infected with EBOV. There are no small molecule therapies to combat EBOV infections. Small molecule antivirals have fewer obstacles associated with cost and delivery and can suppress viral replication in immune-privileged sites.

The EBOV genome is a single-stranded, negative-sense, multicistronic RNA molecule that encodes 7 viral genes. The largest gene, L, is the catalytic subunit of the EBOV viral RNA-dependent RNA polymerase (RdRp), which is essential for replication and expression of the viral RNA genome. L and the viral polymerase cofactor VP35 together form the functional polymerase that acts on the EBOV genome. The viral RNA genome (vRNA) is coated by the viral nucleoprotein (NP), and in concert with the associated RdRp, form the viral ribonucleoprotein complex (vRNP).

Following cell entry, EBOV delivers its vRNP into the host cell cytoplasm where viral replication and transcription take place. Transcription of vRNA by the EBOV polymerase initiates at a single promoter located at the 3'-end of the genome, and discontinuously proceeds through the multicistronic viral genome, stopping at each gene end (GE) signal, which are conserved across all gene borders. At each GE, EBOV polymerase can either reinitiate transcription at the adjacent gene start (GS) signal of the downstream gene, or dissociate and return to the same 3' viral promoter element to initiate a new round of transcription. Thus, EBOV polymerase synthesizes mostly monocistronic viral mRNAs that are present in a progressively decreasing amounts relative to the distance from the promoter due to the transcription attenuation at each gene border. The resulting viral mRNAs can then be translated into viral proteins and sustain progression of the EBOV life cycle. The EBOV polymerase can also adopt a replicase mode, using vRNA as a template to produce a full-length complementary strand (complementary RNA; cRNA), which in

64 turn serves as a template for synthesis of large amounts of NP-coated, progeny viral genomes
65 (Mühlberger, 2007).
66 The underlying mechanisms by which EBOV executes transcriptase and replicase activities
67 are not fully understood, partly due to a lack of structural insight for the full-length EBOV
68 polymerase. For RdRps of other negative-strand RNA viruses for which structural information is
69 available, coordination of multiple domains with distinct enzymatic functions and conformational
70 rearrangement of different domains can endow the viral polymerase with different functions (Te
71 Velthuis et al., 2021). Viral trans-factors can also facilitate function switching (Fearns and Collins,
72 1999; Muhlberger et al., 1999). For instance, the EBOV transcription factor VP30 can recognize
73 non-coding, cis-regulatory sequences within the viral genome and contribute to transcriptase
74 activity of EBOV polymerase (Biedenkopf et al., 2013; Biedenkopf et al., 2016).
75 Here, we asked what role cellular factors might play in modulating distinct steps of viral RNA
76 synthesis mediated by the EBOV polymerase. A previous study examined cellular factors that
77 interact with the EBOV polymerase, but the results were based on over-expression of L in the
78 absence of other needed viral cofactors (Takahashi et al., 2013), which may not have captured the
79 complete functional polymerase interactome. We applied recently developed proximity labeling
80 technologies (Reference) to characterize the cellular interactomes of EBOV polymerase in the
81 context of viral RNA synthesis in living cells. We identified 43 high-confidence candidate interactors
82 of EBOV polymerase in the presence of VP30, and 21 interactors that associate with EBOV
83 polymerase in the absence of VP30. Using a high-content imaging-based siRNA screen with
84 human hepatocyte Huh7 cells infected with authentic EBOV under BSL-4 containment, we
85 confirmed that most of these 21 hits play a functional role in EBOV infection. We focused on one
86 functional interactor, eukaryotic peptide chain release factor subunit 3a (eRF3a/GSPT1), and
87 determined that it physically and functionally associates with the EBOV polymerase. Our results
88 suggest that at early stages of EBOV infection, GSPT1 has an antiviral effect, but at later stages of
89 infection, EBOV hijacks GSPT1 to support viral transcription termination. Our work uncovered a
90 network of host factors that interact with EBOV polymerase and functionally participate in the EBOV
91 life cycle. Further characterization of these host factors can provide new insights into EBOV
92 replication and illuminate novel therapeutic targets for small molecule antiviral development or drug
93 repurposing.
94
95 **RESULTS**
96 **Generating a functional EBOV polymerase with proximity labeling activity.** We selected
97 TurboID, an engineered promiscuous biotin ligase that is optimized for biotinylation of exposed
98 lysine residues on proteins within a ~10 nm radius (Branon et al., 2018). Since the EBOV
99 polymerase (EBOV_pol) requires both L and VP35 proteins to function, we used the split-TurboID

100 system, which was engineered from full-length TurboID to produce two inactive fragments (Cho et
101 al., 2020), sN- and sC-TurboID, that when brought together via protein-protein interactions,
102 reconstitute full-length TurboID and its biotin ligase activity. To construct EBOV L-sNTurboID, we
103 inserted sNTurboID into a predicted flexible loop region in EBOV L, a site that can tolerate insertion
104 of mCherry (Hoenen et al., 2012). To construct EBOV VP35-sCTurboID, we fused the sCTurboID
105 and a HA tag to the EBOV VP35 C terminus, thus preserving the N terminus and internal
106 oligomerization domain, which are implicated in binding to NP and L, respectively, and which are
107 both needed to support viral RNA synthesis (Leung et al., 2015; Moller et al., 2005). Interaction of
108 EBOV L with VP35 upon EBOV_pol formation allows trans-complementation of the associated split-
109 TurboID fragments and biotinylation of neighboring proteins. In addition, the presence of the EBOV
110 transcription factor VP30 can promote conversion of EBOV_pol from a replicase to a transcriptase
111 (Biedenkopf et al., 2013), and likely modulates the polymerase interactome (**Figure 1A**).

112 We confirmed that EBOV_pol split-TurboID fusion is functionally active using an established
113 EBOV viral minigenome (MG) system (Jasenosky et al., 2010a) (**Figure S1**). This MG system
114 recapitulates viral RNA synthesis using a Firefly luciferase reporter as a comprehensive measure
115 of MG replication, transcription, and translation of the MG reporter transcript. As a control, we used
116 wild-type VP35 (VP35-WT) and wild-type L (L-WT). We measured polymerase activity in the
117 presence or absence of VP30, using the activity of WT EBOV_pol (L-VP35 WT) in the presence of
118 VP30 as the standard for normalization. L-WT and C-terminal HA-tagged VP35 (VP35-HA) were
119 compared to VP35-sCTurboID, which served as a control for VP35 expression levels. To increase
120 VP35 expression, we transferred both VP35-HA and VP35-sCTurboID from the original pCEZ to
121 the pCAGGS vector. The EBOV_pol split-TurboID fusion (L-VP35-sTurboID) retains 65% of WT
122 polymerase activity (L-VP35-WT) without noticeable difference in expression levels. The split-
123 TurboID tagged VP35 protein (VP35-sCTurboID) expressed at higher levels than the VP35-HA
124 control. Interestingly, withdrawal of VP30 did not affect activity of either WT or split-TurboID tagged
125 EBOV_pol (**Figure 1B**). This result suggests that, in contrast to other EBOV MG systems
126 (Biedenkopf et al., 2016), the EBOV MG construct we used here permits VP30-independent
127 transcription, a previously described non-canonical transcription mode (Weik et al., 2002). The
128 retention of functional activity by our EBOV MG system without VP30 allows us to probe a context-
129 dependent viral polymerase interactome in the absence of VP30, and downstream validation of
130 VP30-dependent roles of interactors of interest.

131 We validated the proximity labeling activity by detecting biotinylated proteins in cells expressing
132 EBOV_pol split-TurboID fusion together with components of the EBOV MG system. EBOV_pol
133 split-TurboID fusion produced, in a time-dependent manner, a broad range of biotinylated proteins
134 in the presence of exogenous biotin (**Figure 1C&S2**).

135 We used confocal microscopy to detect biotinylation by EBOV_pol split-TurboID fusion in fixed
136 cell specimens. HEK 293T cells transfected with the EBOV MG system, either with the split-TurboID
137 fusion or epitope-tagged EBOV_pol (control) were labeled with biotin for one hour at one day post-
138 transfection. In the absence of a suitable EBOV L-specific monoclonal antibody for
139 immunofluorescence, we used polymerase cofactor VP35 localization as a proxy for EBOV_pol
140 localization. VP35-sCTurboID fluorescence signals were confined inside viral inclusion bodies and
141 overlapped with biotinylation signals. The VP35-HA control was present only at the edges of
142 inclusion bodies and no endogenous biotinylation signal was observed (**Figure 1D**). These different
143 localization patterns of VP35 may be due to the higher expression level of VP35-sTurboID relative
144 to VP35-HA or partitioning of other viral proteins in the EBOV inclusion body, as both phenotypes
145 (inclusion-filling and inclusion-edge) are found in EBOV-infected cells (Nanbo et al., 2013). Most
146 EBOV VP30 did not co-localize with VP35-positive inclusion bodies, but instead formed its own
147 inclusions. The distinct localization is consistent with the VP30-independent EBOV MG activity.

148 **Proximity proteomics to define EBOV polymerase interactomes.** For proximity labeling-based
149 proteomics experiments, we transfected HEK 293T cells with the EBOV MG system components,
150 including wild-type EBOV_pol (WT_pol) or EBOV_pol split-TurboID (sTurboID_pol), followed by
151 biotin labeling. Transfected cells were lysed, and biotinylated proteins were captured with
152 streptavidin (SA) beads that were then subjected to on-bead trypsin digestion. Digested peptides
153 in solution were labeled with unique tandem-mass tags (TMTs) for quantitative proteomics (**Figure**
154 **2A**).
155 To assess enrichment efficiency, biotinylated material bound to SA beads (SA-pull down) from
156 equal amounts of starting material (Input) was eluted in SDS loading buffer and analyzed by
157 western blot (**Figure 2B**). We saw enrichment of biotinylated proteins specific to samples with
158 sTurboID_pol expression compared to those with WT_pol expression. The addition of VP30 to
159 sTurboID_pol appeared to slightly suppress protein expression of both sTurboID_pol and VP30
160 itself, resulting in fewer biotinylated proteins (**Figure 2C**). Both components of EBOV sTurboID_pol
161 were detected in the SA-pull down fraction, suggesting that self-biotinylation occurred.
162 Unexpectedly, the SA-pull down contained no VP30, indicating that it may not directly associate
163 with EBOV L or VP35, or that its spatial localization was outside the labeling radius of sTurboID_pol.
164 Consistent with this finding, we saw no appreciable colocalization of VP30 with VP35-positive
165 inclusion bodies (**Figure 1D**).
166 To analyze EBOV_pol interactomes, we assessed host proteins identified in the proximity
167 interactome by two criteria: degree of enrichment compared to the control proteome (WT_pol), and
168 the corresponding statistical confidence. We normalized the abundance ratio for every protein in
169 the TurboID_pol sample to that in the WT_pol sample and determined the value in terms of fold-
170 change. We then performed multiple comparisons across three biological replicates and

171 determined adjusted *p*-values (adjusted to False Discovery Rate of 0.05) to identify proteins
172 enriched in the TurboID_pol interactome. High-confidence hits were selected using a threshold of
173 adjusted *p-value* < 0.05 and $\log_2$(fold change) > 1. We found 43 high-confidence hits for cellular
174 proteins that interact with the EBOV polymerase in the presence of VP30 (**Figure 2C**). Another 28
175 high-confidence hits were found in the absence of VP30 (**Figure 2D**), 7 of which were the same as
176 those seen in the presence of VP30.

177 **Effect of siRNA targeting high-confidence EBOV polymerase interactors on viral**
178 **infection.** Next, we used an siRNA-based functional screen (Fang et al., 2018) to assess how the
179 EBOV polymerase-interacting protein candidates affected EBOV infection in cultured cells. We
180 transfected human hepatocyte Huh7 cells with individual siRNAs targeting each of 64 high-
181 confidence hits and subsequently infected them with recombinant EBOV-eGFP (Towner et al.,
182 2005). We determined the percentage of GFP-positive cells, as an indicator of EBOV infection, at
183 48 hours post-infection (hpi) (**Figure 3A**). We excluded targets for which depletion significantly
184 altered the cell count, and considered as true hits those having at least two independent siRNA-
185 KD resulting in the same infection phenotype across two experiments.
186 Surprisingly, most high-confidence hits are antiviral, shown by an increased percentage of
187 EBOV-eGFP infection in the presence of siRNA-KD (**Figure 3B**). Limited (10-30% of cells) infection
188 rates for cells transfected with non-silencing control (NSC) siRNA may have favored detection of
189 enhanced infection over reduced infection. However, our results are strongly supported by stringent
190 statistical metrics (two independent experiments with two MOIs, 4 independent siRNAs per target)
191 and are guided by quantitative parameters of the resulting phenotype (i.e., Relative % infection and
192 cell count) (**Figure S3**). We identified 35 potential EBOV-specific antiviral factors (**Figure 3C&D,**
193 **Figure S4**). siRNA knockdown of CKAP5 or RPL18A reduced both EBOV infection and cell count,
194 which prevented their consideration as proviral factors. In contrast, depletion of the EBOV entry
195 receptor NPC1 (positive control) by two individual siRNAs inhibited EBOV infection by nearly 50%,
196 without significantly affecting the cell count (**Figure 3D, top panel)**.
197 Based these results, we highlighted functional interactors identified in the proximity proteomics
198 experiment in an EBOV polymerase interactome network. We clustered all polymerase interactors
199 based on their STRING-classified biological processes (Szklarczyk et al., 2019). Many interactors
200 are involved in critical cellular pathways that could be functionally involved in the EBOV life cycle
201 (**Figure 4A**).

202 **GSPT1 is functionally relevant to EBOV RNA synthesis.** Two functional polymerase interactors,
203 UPF1 and GSPT1, are both key components of the cellular nonsense mRNA decay (NMD)
204 pathway. UPF1 restricts infection by multiple RNA viruses (May and Simon, 2021), whereas GSPT1
205 has not been implicated in viral infections. Thus, as a proof-of-principle, we focused on GSPT1,

206 which is a translation termination factor that is also termed eRF3a, eukaryotic peptide chain release
207 factor GTP-binding subunit (Zhouravleva et al., 1995).
208 First, we used co-immunoprecipitation (co-IP) assays to verify whether GSPT1 indeed physically
209 interacts with EBOV polymerase (EBOV_pol). Using HEK 293T cells co-expressing an N-terminal
210 Flag-tagged GSPT1 (long isoform, 68.7KDa) and EBOV polymerase components, either
211 individually or in combination, we found that L-WT, in the presence of VP35-HA, consistently co-
212 IPs with Flag-GSPT1 (**Figure 5A)**. However, Flag-GSPT1 did not co-IP with the VP35-HA
213 component of EBOV_pol (**Figure 5B,** left panel**)**. Interestingly, we observed a pronounced
214 degradation product of L-WT in the input cell lysate but not the co-IP fraction, suggesting that the
215 interaction between Flag-GSPT1 and EBOV L-WT requires full-length L (or at least the presence
216 of regions otherwise subject to degradation). In addition, EBOV VP30 associates with Flag-GSPT1
217 only in the presence of EBOV_pol; VP30 alone does not associate with GSPT1 (**Figure 5A&B,**
218 right panel). L, VP35 and VP30 all bind RNA, but GSPT1 is not known to have RNA-binding activity.
219 Therefore, the GSPT1-EBOV protein-protein interactions we detected are likely not due to indirect
220 interactions bridged by RNA.
221 We next examined whether endogenous GSPT1 interacts with EBOV_pol in a cellular context
222 that recapitulates viral RNA synthesis. In HEK 293T cells transfected with the components of the
223 EBOV MG system, we observed a specific pattern of GSPT1 clusters in the cytoplasm that appear
224 to contact EBOV VP35-positive inclusion bodies (**Figure 5C,** top panel). In control cells, however,
225 endogenous GSPT1 has a mostly diffuse nucleocytoplasmic distribution, with sporadic clusters
226 occasionally observed (**Figure 5C,** bottom panel). Accordingly, we determined the functional
227 consequence of GSPT1 association with EBOV_pol using the EBOV MG assay. Consistent with
228 the siRNA screen results, over-expression or GSPT1 knockdown (KD) significantly decreases and
229 increases, respectively, EBOV MG activity. Meanwhile, changes in GSPT1 expression level did not
230 significantly affect expression of a control eGFP-reporter (**Figure 5C&S5**). Together, our data
231 suggest that GSPT1 is a *bona fide* EBOV polymerase interactor that may participate in EBOV viral
232 RNA synthesis.

233 **Hijacking of GSPT1 by EBOV to facilitate transcription termination.** For the siRNA screen we
234 measured viral infection at a single time point (48 hours post-infection). Thus, we sought to further
235 validate the phenotype of GSPT1-KD by following the multi-step EBOV growth kinetics in Huh7
236 cells. We first confirmed that GSPT1-KD persisted for 7 days post-siRNA transfection, supporting
237 that a reduction in endogenous GSPT1 would be likely sustained throughout the 4-day viral growth
238 curve experiments (**Figure S5**). We infected GSPT1-KD cells with EBOV and measured viral titers
239 in the cell supernatant on 4 consecutive days. We quantified viral RNA and protein levels in infected
240 cell lysates, and imaged infected monolayers at the experiment endpoint.

241 Intriguingly, GSPT1-KD initially increased EBOV titers by 2- to 4-fold relative to the non-silencing
242 control (NSC). However, at 3- and 4-days post-infection (dpi), GSPT1-KD correlated with reduced
243 EBOV titers (**Figure 6A**). At 4 dpi, we observed an increase in EBOV NP mRNA accumulation, with
244 a marginal decrease in EBOV vRNA accumulation (**Figure 6B&C**). Despite the increase in viral
245 mRNA, viral protein levels, including EBOV glycoprotein subunit 2 (GP2), were reduced, and fewer
246 EBOV-infected cells were seen with GSPT1-KD (**Figure 6C&D**). Notably, we observed that EBOV
247 infection triggered a significant upregulation of GSPT1 mRNA levels (**Figure 6E**), and the
248 appearance of a lower-molecular weight GSPT1 species (~40kDa) that could correspond to a
249 cleavage product of GSPT1 (**Figure 6C**). These findings suggest virus-specific, time-dependent
250 regulation of GSPT1 protein levels.
251 GSPT1 antiviral activity during the first 48 hours of EBOV infection could be linked to the role of
252 GSPT1 in the cellular NMD pathway (Hoshino, 2012). The NMD pathway often targets viral mRNAs
253 for degradation and thereby restricts growth of many RNA viruses, some of which evolved
254 mechanisms to evade this host restriction (Balistreri et al., 2017). EBOV infection induced
255 upregulation of GSPT1 and appearance of the GSPT1 cleavage product is consistent with EBOV
256 antagonizing GSPT1-assisted, post-transcriptional elimination of viral mRNAs. However, the
257 observed increase in EBOV mRNA levels does not translate into increased accumulation of any
258 viral protein, suggesting that GSPT1 may play another role in the EBOV life cycle.
259 The concurrent increase in EBOV mRNAs and decrease in EBOV protein accumulation might
260 reflect aberrant transcription triggered by GSPT1-KD. For the multicistronic EBOV genome, one
261 type of aberrant transcription is read-through mRNA synthesis, which occurs when the viral
262 polymerase reads-through the transcription termination signal of an upstream gene to continue
263 transcribing the downstream gene unit (Brauburger et al., 2014). The outcome of readthrough
264 mRNA synthesis can be an apparent increase in EBOV mRNA levels that is associated with fewer
265 transcription attenuation steps and accompanied by decreased viral translation of the downstream
266 genes in the readthrough mRNAs.
267 The accumulation of all EBOV mRNAs we measured was increased upon GSPT1-KD. However,
268 the magnitude of this increase was greater for genes located on the promoter-distal, 5' end of the
269 EBOV genome, compared to genes on the promoter-proximal, 3' end at the polymerase entry site
270 (**Figure 6F&G**). Accordingly, in GSPT1-depleted cells, we detected higher incidence of EBOV
271 transcription read-through in 3 of the 4 gene borders we examined that were marked by the
272 detection of mRNAs containing gene junction sequences derived from two adjacent transcription
273 units (**Figure 6F&H**). However, GSPT1-KD did not appear to affect transcription readthrough at the
274 VP24/L gene border. Further, we observed varying degrees of reduction in accumulation of 6 viral
275 proteins upon GSPT1-KD (**Figure 6I**). Together, these results indicate that at later times of viral

276 infection, GSPT1 can be hijacked by the EBOV polymerase to facilitate a critical step of the highly
277 regulated viral transcription process and modulate the level of individual EBOV mRNAs.

278 **DISCUSSION**

279 Here we present the first systematic analysis of the EBOV polymerase-cellular interactome in
280 the context of viral RNA synthesis. We used proximity-labeling to characterize the EBOV
281 polymerase interactomes *in situ,* and performed an siRNA screen in human hepatocytes infected
282 with EBOV to identify functionally important interactors with EBOV polymerase during EBOV
283 infection. We discovered 64 high-confidence EBOV polymerase interactors, 31 of which were
284 validated by our siRNA screen as functional hits. Most polymerase-interactors we identified are
285 antiviral rather than proviral, suggesting that the viral polymerase, or viral RNA products, or both,
286 are targets of host innate defense mechanisms. As a proof-of-principle, we chose one functional
287 hit, GSPT1, to further dissect the interplay between EBOV polymerase and this host factor. GSPT1
288 appeared to play antiviral role in concert with another host factor, UPF1, in mediating RNA decay.
289 However, our data indicated that EBOV can in turn recruit GSPT1 to assist in highly regulated viral
290 transcription.

291 We identified 12 EBOV polymerase interactors that were previously shown by various
292 approaches, most involving traditional affinity-purification mass spectrometry (AP-MS), to be
293 components of the EBOV-host interactome (**Figure 4B**) (Fan et al., 2020; Garcia-Dorival et al.,
294 2016; Morwitzer et al., 2019; Spurgers et al., 2010; Takahashi et al., 2013). To avoid using cells
295 infected with authentic EBOV, which requires Biosafety level-4 (BSL4) containment, these
296 proteomic experiments typically used cells overexpressing a single viral bait protein. Such bait
297 proteins and protein-protein interactions analyzed in AP-MS experiments must be stable to facilitate
298 affinity-purification and analysis. However, the EBOV polymerase can be unstable and interactions
299 between EBOV polymerase and other cellular or viral factors can be dynamic. To capture both
300 stable and dynamic protein interactions, here we used a proximity-labeling approach involving split-
301 TurboID with an EBOV minigenome (MG) system that incorporates all the molecular components
302 relevant to the EBOV polymerase activity and recapitulates EBOV RNA synthesis events. This
303 system also allowed us to compare the cellular interactome of EBOV polymerase in the absence
304 or presence of the EBOV VP30, which is essential viral cofactor for transcription, but not replication,
305 of the viral genome.

306 In the absence of VP30, we identified eight functional hits that interacted with EBOV polymerase,
307 of which three are implicated in other viral infections. ZC3H7A interacts with SARS-CoV2
308 polymerase and negatively regulates pan-coronavirus infection (Hoffmann et al., 2021); HNRNPA1
309 interacts with Hepatitis C virus (HCV) polymerase to regulate HCV replication (Kim et al., 2007;
310 Rios-Marco et al., 2016); and MRE11 acts as a cytosolic dsDNA sensor that activates the STING
311 pathway during Herpes simplex virus infection (Kondo et al., 2013). Our siRNA screen indicated

312 that these same host factors can also suppress EBOV infection, suggesting that there may be a
313 conserved panel of host restriction factors that respond to infection with various viral pathogens.
314 Among the eight hits, we also identified the dsRNA sensor EIF2AK2/PKR, which was previously
315 shown to be antagonized by EBOV VP35 (Feng et al., 2007; Schumann et al., 2009).
316 In the presence of VP30, we found 19 functional hits specific to EBOV polymerase. These hits
317 are functionally enriched in four biological processes, including cytoskeleton organization (DOCK7,
318 CTTN, CORO7, CNN3, AMOT, FLNA), chaperone-mediated protein folding (UNC45A and CCT8),
319 negative regulation of translation (EIF4E2 and GIGYF2) and RNA catabolic processes (UPF1 and
320 GSPT1). Certain cytoskeleton re-organizations might be associated with growth of EBOV inclusion
321 bodies, which can consume a significant portion of the cytoplasmic space as infection progresses
322 (Hoenen et al., 2012; Nanbo et al., 2013). Future work is needed to address whether these host
323 factors restrict expansion of EBOV inclusion bodies to suppress viral infection. Interestingly,
324 EIF4E2 and GIGYF2, a translation repression complex, can both suppress cap-dependent
325 translation of specific mRNAs (Peter et al., 2017), and interact with SARS-CoV2 NSP2 to enhance
326 SARS-CoV2 infection (Hoffmann et al., 2021). In contrast, we found that EIF4E2 and GIGYF2
327 antagonize EBOV infection, suggesting that viral mRNA features unique to each virus might
328 account for the differential regulation by EIF4E2-GIGYF2 complex during viral infection.
329 Here we discovered two critical players in the cellular nonsense-mediated decay (NMD)
330 pathway, UPF1 and GSPT1, which can both regulate EBOV infection. Although the role of NMD
331 decay in virus infection has been examined for positive-strand and double-strand RNA viruses,
332 retroviruses and influenza (Balistreri et al., 2017; Declercq et al., 2020; Popp et al., 2020; Tran et
333 al., 2021), how NMD affects negative-strand RNA viruses like EBOV that replicate in the cytoplasm
334 remains unclear. In the cellular NMD pathway, UPF1 degrades aberrant mRNAs by binding to the
335 translation-termination complex (GSPT1/eRF3-eRF1) upon ribosomal recognition of a premature
336 termination codon (PTC) in the mRNA (Kurosaki and Maquat, 2016). After recruitment to the
337 termination complex, UPF1 is phosphorylated by SMG1, which facilitates recruitment of other
338 cellular factors to dismantle the target transcript (Kurosaki et al., 2019). EBOV mRNAs likely
339 incorporate PTCs owing to the presence of upstream open reading frames (uORF). Indeed, the 5'
340 untranslated region (UTR) of 4 of the 7 EBOV mRNAs contain upstream AUGs (Shabman et al.,
341 2013) that can lead to uORF expression and triggering of UPF1-mediated mRNA decay. Our siRNA
342 screen indicated that UPF1 can restrict EBOV infection, but whether it directly targets EBOV
343 mRNAs for degradation, whether it is a conserved host antiviral defense mechanism to limit
344 negative-strand RNA virus infection, and/or whether EBOV can evade host responses by the UPF1-
345 assisted NMD pathway remain to be determined.
346 GSPT1 is a core component of translation termination machinery (Frolova et al., 1996;
347 Zhouravleva et al., 1995) and triggers the NMD pathway through interactions with UPF1. GSPT1

348 also regulates cell cycle progression (Chauvin et al., 2007) and promotes apoptosis (Hegde et al.,
349 2003). This participation in multiple cellular pathways suggests that GSPT1 may regulate viral
350 infection in different ways in a context-dependent manner.

351 We observed an antiviral role for GSPT1 in EBOV infection in our siRNA screen. We confirmed
352 this antiviral role of GSPT1 in a monocistronic EBOV MG system, as well as in production of
353 infectious progeny 1- to 2- days after viral infection. Together with our finding that EBOV mRNA
354 accumulation increased upon GSPT1-KD, EBOV mRNAs could be negatively regulated by the
355 GSPT1-dependent NMD pathway that may also involve UPF1. However, further studies are
356 needed to determine the interplay between GSPT1-dependent mRNA decay and EBOV mRNA
357 accumulation.

358 Multiple lines of evidence demonstrated that at later times of infection, EBOV can counteract
359 GSPT1-mediated restrictions and hijack GSPT1 to facilitate viral infection. The physical interaction
360 of GSPT1 with EBOV polymerase and VP30 suggests that GSPT1 may participate in EBOV
361 transcription, a process that follows a “stop-start” model, in which the viral polymerase starts
362 transcription at the 3' promoter region and proceeds discontinuously through the viral genome to
363 synthesize a gradient of viral mRNAs (Hume and Muhlberger, 2019). EBOV transcription is
364 regulated by the conserved gene start (GS) and gene end (GE) sequences flanking each ORF, as
365 well as, in some cases, intergenic regions (IGRs) separating two adjacent genes. Failure to
366 recognize GEs can lead to read-though mRNAs that may not be correctly translated by the host
367 ribosome (Brauburger et al., 2014). Our results support an enhanced-read-through phenotype in
368 that we saw both a disproportionate increase in viral mRNAs and concomitant increased
369 occurrence of readthrough mRNAs with GSPT1-KD. Interestingly, we detected transcriptional
370 readthrough occurring at the VP24/L gene border, although at a lower frequency compared to other
371 gene borders, but this readthrough is not affected by GSPT1-KD. This observation might correlate
372 with the two consecutive VP24 GE signals located in the VP24/L gene border and the reinforced
373 inhibitory effect on transcription read-through.

374 As a result, translation efficiency of ORFs located downstream within read-through viral mRNAs
375 is decreased, leading to fewer copies of viral proteins and in turn attenuated virus particle
376 production (**Figure 6 A, I &H**). The monocistronic EBOV minigenome (MG) system we used cannot
377 recapitulate readthrough events, and therefore the decreased EBOV MG activity when GSPT1 is
378 overexpressed could reflect increased NMD suppression (**Figure 5C**). Future studies using a
379 multicistronic EBOV MG system that recapitulates EBOV transcription read-through may clarify the
380 supporting role that GSPT1 may play in EBOV transcription termination. As with other
381 mononegaviruses including vesicular stomatitis virus (VSV) (Barr et al., 2002) and respiratory
382 syncytial virus (RSV) (Fearns and Collins, 1999), EBOV transcription is regulated by *cis*-acting
383 elements in the viral genome, including 3' transcription promoter elements, GSs, GEs and IGRs

384 (Biedenkopf et al., 2016; Brauburger et al., 2014; Muhlberger et al., 1999; Weik et al., 2002).
385 Studies examining EBOV transcription regulation have largely focused on the virus-encoded, *trans*-
386 acting factor VP30 and its role in activating EBOV transcription initiation. Our study, for the first
387 time, revealed a possible mechanism for EBOV transcription regulation that involves a host *trans*-
388 acting factor in EBOV transcription termination. How the GSPT1-assisted transcription termination
389 coordinates with the *cis*-acting elements in the EBOV genome remains unclear. Based on the
390 similarity of transcription regulation shared with other mononegaviruses, GSPT1 might also support
391 transcription termination of other related viruses and thus GPST1-assisted transcription termination
392 could be a pharmacological target to abrogate viral infection. Combined with the observation that
393 EBOV infection can modulate endogenous levels of GSPT1 and its protein integrity, EBOV
394 polymerase may engage GSPT1-mediated regulation of synthesis of individual EBOV mRNAs to
395 fine-tune viral infection.
396 In summary, we present a comprehensive proximity interactome of EBOV polymerase attained
397 in the context of a reconstituted, functional vRNP replication unit and validated the functional role
398 of individual EBOV polymerase interactors in an siRNA-screen with authentic EBOV infection. As
399 a proof-of-concept, we characterized the mechanisms of action for one novel host factor, GSPT1,
400 in the transcriptional and post-transcriptional regulation of EBOV mRNA synthesis. Further work is
401 needed to explore the role of other functional interactors in EBOV infection that we identified and
402 to confirm their functional importance in other primary target cells including macrophage and
403 dendritic cells. Together, our findings illuminate new mechanisms of host regulation of EBOV
404 replication and reveal a landscape of novel targets for host-derived antiviral development.
405
406 **ACKNOWLEDGMENTS**
407 We thank Jonathan Towner (CDC) and Stuart Nichol (CDC) for providing the EBOV full-length
408 clone, Yoshihiro Kawaoka (University of Wisconsin) for providing the pCEZ-NP, VP35, L, VP30,
409 and the pHH21-3E5E-Fluc plasmids, as well as sharing the anti-VP30 antibody. We thank Beatrice
410 Cubitt from the de la Torre Lab (Scripps Research, CA) for helping with cloning of pCI-FLAG-
411 GSPT1 plasmid. We thank Diptiben Parekh (LJI) for plasmid preparations, Sharon Schendel (LJI)
412 for manuscript editing, Zbigniew Mikulski of the Microscopy Core Facility (LJI) for microscopy
413 training, and NIH S10OD021831 for sponsoring the Zeiss LSM 880 microscope. This research was
414 supported by institutional funds of La Jolla Institute for Immunology. J.F. was supported by the
415 Donald E. and Delia B. Baxter Foundation Fellowship.
416
417 **AUTHOR CONTRIBUTIONS**
418 J.F., J.C.T., and E.O.S. designed research and wrote the paper; J.F. performed all non-BSL4
419 experiments and analyzed data; C.P. performed all BSL-4 experiments; A.B. provided supervision

420 for BSL-4 research; G.T. and G.C performed proteomic experiments and analyses; K.F.C. and
421 A.Y.T provided a critical resource; all authors edited and approved the paper.
422
423 **DECLARATION OF INTERESTS**
424 The authors declare no competing interest.
425
426 **REFERENCES**

427 Adekanmbi, O., Ilesanmi, O., and Lakoh, S. (2021). Ebola: A review and focus on neurologic
428 manifestations. J Neurol Sci *421*, 117311.
429 Balistreri, G., Bognanni, C., and Muhlemann, O. (2017). Virus Escape and Manipulation of
430 Cellular Nonsense-Mediated mRNA Decay. Viruses *9*.
431 Barr, J.N., Whelan, S.P., and Wertz, G.W. (2002). Transcriptional control of the RNA-dependent
432 RNA polymerase of vesicular stomatitis virus. Biochim Biophys Acta *1577*, 337-353.
433 Biedenkopf, N., Hartlieb, B., Hoenen, T., and Becker, S. (2013). Phosphorylation of Ebola virus
434 VP30 influences the composition of the viral nucleocapsid complex: impact on viral transcription
435 and replication. J Biol Chem *288*, 11165-11174.
436 Biedenkopf, N., Schlereth, J., Grunweller, A., Becker, S., and Hartmann, R.K. (2016). RNA Binding
437 of Ebola Virus VP30 Is Essential for Activating Viral Transcription. J Virol *90*, 7481-7496.
438 Branon, T.C., Bosch, J.A., Sanchez, A.D., Udeshi, N.D., Svinkina, T., Carr, S.A., Feldman, J.L.,
439 Perrimon, N., and Ting, A.Y. (2018). Efficient proximity labeling in living cells and organisms with
440 TurboID. Nat Biotechnol *36*, 880-887.
441 Brauburger, K., Boehmann, Y., Tsuda, Y., Hoenen, T., Olejnik, J., Schumann, M., Ebihara, H., and
442 Muhlberger, E. (2014). Analysis of the highly diverse gene borders in Ebola virus reveals a
443 distinct mechanism of transcriptional regulation. J Virol *88*, 12558-12571.
444 Chauvin, C., Salhi, S., and Jean-Jean, O. (2007). Human eukaryotic release factor 3a depletion
445 causes cell cycle arrest at G1 phase through inhibition of the mTOR pathway. Mol Cell Biol *27*,
446 5619-5629.
447 Cho, K.F., Branon, T.C., Rajeev, S., Svinkina, T., Udeshi, N.D., Thoudam, T., Kwak, C., Rhee, H.W.,
448 Lee, I.K., Carr, S.A.*, et al.* (2020). Split-TurboID enables contact-dependent proximity labeling in
449 cells. Proc Natl Acad Sci U S A *117*, 12143-12154.

450 Declercq, M., Biquand, E., Karim, M., Pietrosemoli, N., Jacob, Y., Demeret, C., Barbezange, C.,
451 and van der Werf, S. (2020). Influenza A virus co-opts ERI1 exonuclease bound to histone mRNA
452 to promote viral transcription. Nucleic Acids Res *48*, 10428-10440.
453 Eghrari, A.O., Bishop, R.J., Ross, R.D., Davis, B., Larbelee, J., Amegashie, F., Dolo, R.F.,
454 Prakalapakorn, S.G., Gaisie, C., Gargu, C.*, et al.* (2021). Characterization of Ebola Virus-
455 Associated Eye Disease. JAMA Netw Open *4*, e2032216.
456 Fan, J., Liu, X., Mao, F., Yue, X., Lee, I., and Xu, Y. (2020). Proximity proteomics identifies novel
457 function of Rab14 in trafficking of Ebola virus matrix protein VP40. Biochem Biophys Res
458 Commun *527*, 387-392.
459 Fang, J., Pietzsch, C., Ramanathan, P., Santos, R.I., Ilinykh, P.A., Garcia-Blanco, M.A., Bukreyev,
460 A., and Bradrick, S.S. (2018). Staufen1 Interacts with Multiple Components of the Ebola Virus
461 Ribonucleoprotein and Enhances Viral RNA Synthesis. mBio *9*.
462 Fatscher, T., Boehm, V., Weiche, B., and Gehring, N.H. (2014). The interaction of cytoplasmic
463 poly(A)-binding protein with eukaryotic initiation factor 4G suppresses nonsense-mediated
464 mRNA decay. RNA *20*, 1579-1592.
465 Fearns, R., and Collins, P.L. (1999). Role of the M2-1 transcription antitermination protein of
466 respiratory syncytial virus in sequential transcription. J Virol *73*, 5852-5864.
467 Feng, Z., Cerveny, M., Yan, Z., and He, B. (2007). The VP35 protein of Ebola virus inhibits the
468 antiviral effect mediated by double-stranded RNA-dependent protein kinase PKR. J Virol *81*, 182-
469 192.
470 Fatscher, T., Boehm, V., Weiche, B., and Gehring, N.H. (2014). The interaction of cytoplasmic
471 poly(A)-binding protein with eukaryotic initiation factor 4G suppresses nonsense-mediated
472 mRNA decay. RNA 20, 1579-1592.
473 Flyak, A.I., Kuzmina, N., Murin, C.D., Bryan, C., Davidson, E., Gilchuk, P., Gulka, C.P., Ilinykh, P.A.,
474 Shen, X., Huang, K.*, et al.* (2018). Broadly neutralizing antibodies from human survivors target a
475 conserved site in the Ebola virus glycoprotein HR2-MPER region. Nat Microbiol *3*, 670-677.
476 Frolova, L., Le Goff, X., Zhouravleva, G., Davydova, E., Philippe, M., and Kisselev, L. (1996).
477 Eukaryotic polypeptide chain release factor eRF3 is an eRF1- and ribosome-dependent
478 guanosine triphosphatase. RNA *2*, 334-341.

479 Garcia-Dorival, I., Wu, W., Armstrong, S.D., Barr, J.N., Carroll, M.W., Hewson, R., and Hiscox, J.A.
480 (2016). Elucidation of the Cellular Interactome of Ebola Virus Nucleoprotein and Identification of
481 Therapeutic Targets. J Proteome Res *15*, 4290-4303.
482 Hegde, R., Srinivasula, S.M., Datta, P., Madesh, M., Wassell, R., Zhang, Z., Cheong, N., Nejmeh, J.,
483 Fernandes-Alnemri, T., Hoshino, S.*, et al.* (2003). The polypeptide chain-releasing factor
484 GSPT1/eRF3 is proteolytically processed into an IAP-binding protein. J Biol Chem *278*, 38699-
485 38706.
486 Hoenen, T., Shabman, R.S., Groseth, A., Herwig, A., Weber, M., Schudt, G., Dolnik, O., Basler,
487 C.F., Becker, S., and Feldmann, H. (2012). Inclusion bodies are a site of ebolavirus replication. J
488 Virol *86*, 11779-11788.
489 Hoffmann, H.H., Sanchez-Rivera, F.J., Schneider, W.M., Luna, J.M., Soto-Feliciano, Y.M.,
490 Ashbrook, A.W., Le Pen, J., Leal, A.A., Ricardo-Lax, I., Michailidis, E.*, et al.* (2021). Functional
491 interrogation of a SARS-CoV-2 host protein interactome identifies unique and shared
492 coronavirus host factors. Cell Host Microbe *29*, 267-280 e265.
493 Hoshino, S. (2012). Mechanism of the initiation of mRNA decay: role of eRF3 family G proteins.
494 Wiley Interdiscip Rev RNA *3*, 743-757.
495 Hume, A.J., and Muhlberger, E. (2019). Distinct Genome Replication and Transcription Strategies
496 within the Growing Filovirus Family. J Mol Biol *431*, 4290-4320.
497 Jasenosky, L.D., Neumann, G., and Kawaoka, Y. (2010a). Minigenome-based reporter system
498 suitable for high-throughput screening of compounds able to inhibit Ebolavirus replication
499 and/or transcription. Antimicrob Agents Chemother *54*, 3007-3010.
500 Jasenosky, L.D., Neumann, G., and Kawaoka, Y. (2010b). Minigenome-based reporter system
501 suitable for high-throughput screening of compounds able to inhibit Ebolavirus replication
502 and/or transcription. Antimicrob Agents Chemother *54*, 3007-3010.
503 Kim, C.S., Seol, S.K., Song, O.K., Park, J.H., and Jang, S.K. (2007). An RNA-binding protein, hnRNP
504 A1, and a scaffold protein, septin 6, facilitate hepatitis C virus replication. J Virol *81*, 3852-3865.
505 Kondo, T., Kobayashi, J., Saitoh, T., Maruyama, K., Ishii, K.J., Barber, G.N., Komatsu, K., Akira, S.,
506 and Kawai, T. (2013). DNA damage sensor MRE11 recognizes cytosolic double-stranded DNA and
507 induces type I interferon by regulating STING trafficking. Proc Natl Acad Sci U S A *110*, 2969-
508 2974.

509 Kurosaki, T., and Maquat, L.E. (2016). Nonsense-mediated mRNA decay in humans at a glance. J
510 Cell Sci *129*, 461-467.
511 Kurosaki, T., Popp, M.W., and Maquat, L.E. (2019). Quality and quantity control of gene
512 expression by nonsense-mediated mRNA decay. Nat Rev Mol Cell Biol *20*, 406-420.
513 Leung, D.W., Borek, D., Luthra, P., Binning, J.M., Anantpadma, M., Liu, G., Harvey, I.B., Su, Z.,
514 Endlich-Frazier, A., Pan, J.*, et al.* (2015). An Intrinsically Disordered Peptide from Ebola Virus
515 VP35 Controls Viral RNA Synthesis by Modulating Nucleoprotein-RNA Interactions. Cell Rep *11*,
516 376-389.
517 May, J.P., and Simon, A.E. (2021). Targeting of viral RNAs by Upf1-mediated RNA decay
518 pathways. Curr Opin Virol *47*, 1-8.
519 Moller, P., Pariente, N., Klenk, H.D., and Becker, S. (2005). Homo-oligomerization of
520 Marburgvirus VP35 is essential for its function in replication and transcription. J Virol *79*, 14876-
521 14886.
522 Morwitzer, M.J., Tritsch, S.R., Cazares, L.H., Ward, M.D., Nuss, J.E., Bavari, S., and Reid, S.P.
523 (2019). Identification of RUVBL1 and RUVBL2 as Novel Cellular Interactors of the Ebola Virus
524 Nucleoprotein. Viruses *11*.
525 Mühlberger, E. (2007). Filovirus replication and transcription. *2*, 205-215.
526 Muhlberger, E., Weik, M., Volchkov, V.E., Klenk, H.D., and Becker, S. (1999). Comparison of the
527 transcription and replication strategies of marburg virus and Ebola virus by using artificial
528 replication systems. J Virol *73*, 2333-2342.
529 Nanbo, A., Watanabe, S., Halfmann, P., and Kawaoka, Y. (2013). The spatio-temporal distribution
530 dynamics of Ebola virus proteins and RNA in infected cells. Sci Rep *3*, 1206.
531 Peter, D., Weber, R., Sandmeir, F., Wohlbold, L., Helms, S., Bawankar, P., Valkov, E., Igreja, C.,
532 and Izaurralde, E. (2017). GIGYF1/2 proteins use auxiliary sequences to selectively bind to 4EHP
533 and repress target mRNA expression. Genes Dev *31*, 1147-1161.
534 Popp, M.W., Cho, H., and Maquat, L.E. (2020). Viral subversion of nonsense-mediated mRNA
535 decay. RNA *26*, 1509-1518.
536 Rios-Marco, P., Romero-Lopez, C., and Berzal-Herranz, A. (2016). The cis-acting replication
537 element of the Hepatitis C virus genome recruits host factors that influence viral replication and
538 translation. Sci Rep *6*, 25729.

539 Schindelin, J., Arganda-Carreras, I., Frise, E., Kaynig, V., Longair, M., Pietzsch, T., Preibisch, S.,
540 Rueden, C., Saalfeld, S., Schmid, B.*, et al.* (2012). Fiji: an open-source platform for biological-
541 image analysis. Nat Methods *9*, 676-682.
542 Schindelin, J., Arganda-Carreras, I., Frise, E., Kaynig, V., Longair, M., Pietzsch, T., Preibisch, S.,
543 Rueden, C., Saalfeld, S., Schmid, B., et al. (2012). Fiji: an open-source platform for biological-
544 image analysis. Nat Methods 9, 676-682.
545 Schneider, C.A., Rasband, W.S., and Eliceiri, K.W. (2012). NIH Image to ImageJ: 25 years of image
546 analysis. Nat Methods *9*, 671-675.
547 Schumann, M., Gantke, T., and Muhlberger, E. (2009). Ebola virus VP35 antagonizes PKR activity
548 through its C-terminal interferon inhibitory domain. J Virol *83*, 8993-8997.
549 Shabman, R.S., Hoenen, T., Groseth, A., Jabado, O., Binning, J.M., Amarasinghe, G.K., Feldmann,
550 H., and Basler, C.F. (2013). An upstream open reading frame modulates ebola virus polymerase
551 translation and virus replication. PLoS Pathog *9*, e1003147.
552 Spurgers, K.B., Alefantis, T., Peyser, B.D., Ruthel, G.T., Bergeron, A.A., Costantino, J.A., Enterlein,
553 S., Kota, K.P., Boltz, R.C., Aman, M.J.*, et al.* (2010). Identification of essential filovirion-associated
554 host factors by serial proteomic analysis and RNAi screen. Mol Cell Proteomics *9*, 2690-2703.
555 Szklarczyk, D., Gable, A.L., Lyon, D., Junge, A., Wyder, S., Huerta-Cepas, J., Simonovic, M.,
556 Doncheva, N.T., Morris, J.H., Bork, P.*, et al.* (2019). STRING v11: protein-protein association
557 networks with increased coverage, supporting functional discovery in genome-wide
558 experimental datasets. Nucleic Acids Res *47*, D607-D613.
559 Takahashi, K., Halfmann, P., Oyama, M., Kozuka-Hata, H., Noda, T., and Kawaoka, Y. (2013). DNA
560 topoisomerase 1 facilitates the transcription and replication of the Ebola virus genome. J Virol
561 *87*, 8862-8869.
562 Te Velthuis, A.J.W., Grimes, J.M., and Fodor, E. (2021). Structural insights into RNA polymerases
563 of negative-sense RNA viruses. Nat Rev Microbiol *19*, 303-318.
564 Ting, L., Rad, R., Gygi, S.P., and Haas, W. (2011). MS3 eliminates ratio distortion in isobaric
565 multiplexed quantitative proteomics. Nat Methods *8*, 937-940.
566 Towner, J.S., Paragas, J., Dover, J.E., Gupta, M., Goldsmith, C.S., Huggins, J.W., and Nichol, S.T.
567 (2005). Generation of eGFP expressing recombinant Zaire ebolavirus for analysis of early
568 pathogenesis events and high-throughput antiviral drug screening. Virology *332*, 20-27.

569 Tran, G.V.Q., Kleinehr, J., Preugschas, H.F., Anhlan, D., Mohamed, F.F., Ehrhardt, C., Ludwig, S.,
570 and Hrincius, E.R. (2021). Nonsense-mediated mRNA decay does not restrict influenza A virus
571 propagation. Cell Microbiol *23*, e13323.
572 Weik, M., Modrof, J., Klenk, H.D., Becker, S., and Muhlberger, E. (2002). Ebola virus VP30-
573 mediated transcription is regulated by RNA secondary structure formation. J Virol *76*, 8532-
574 8539.
575 Xu, M.J., Stanford-Moore, G., and Czechowicz, J.A. (2019). Association of Ebola Virus Infection
576 With Hearing Loss in Regions Where Ebola Virus Infection Is Endemic: A Systematic Review.
577 JAMA Otolaryngol Head Neck Surg *145*, 669-675.
578 Zhouravleva, G., Frolova, L., Le Goff, X., Le Guellec, R., Inge-Vechtomov, S., Kisselev, L., and
579 Philippe, M. (1995). Termination of translation in eukaryotes is governed by two interacting
580 polypeptide chain release factors, eRF1 and eRF3. EMBO J *14*, 4065-4072.

581

582

583

584 **FIGURE TITLES AND LEGENDS**

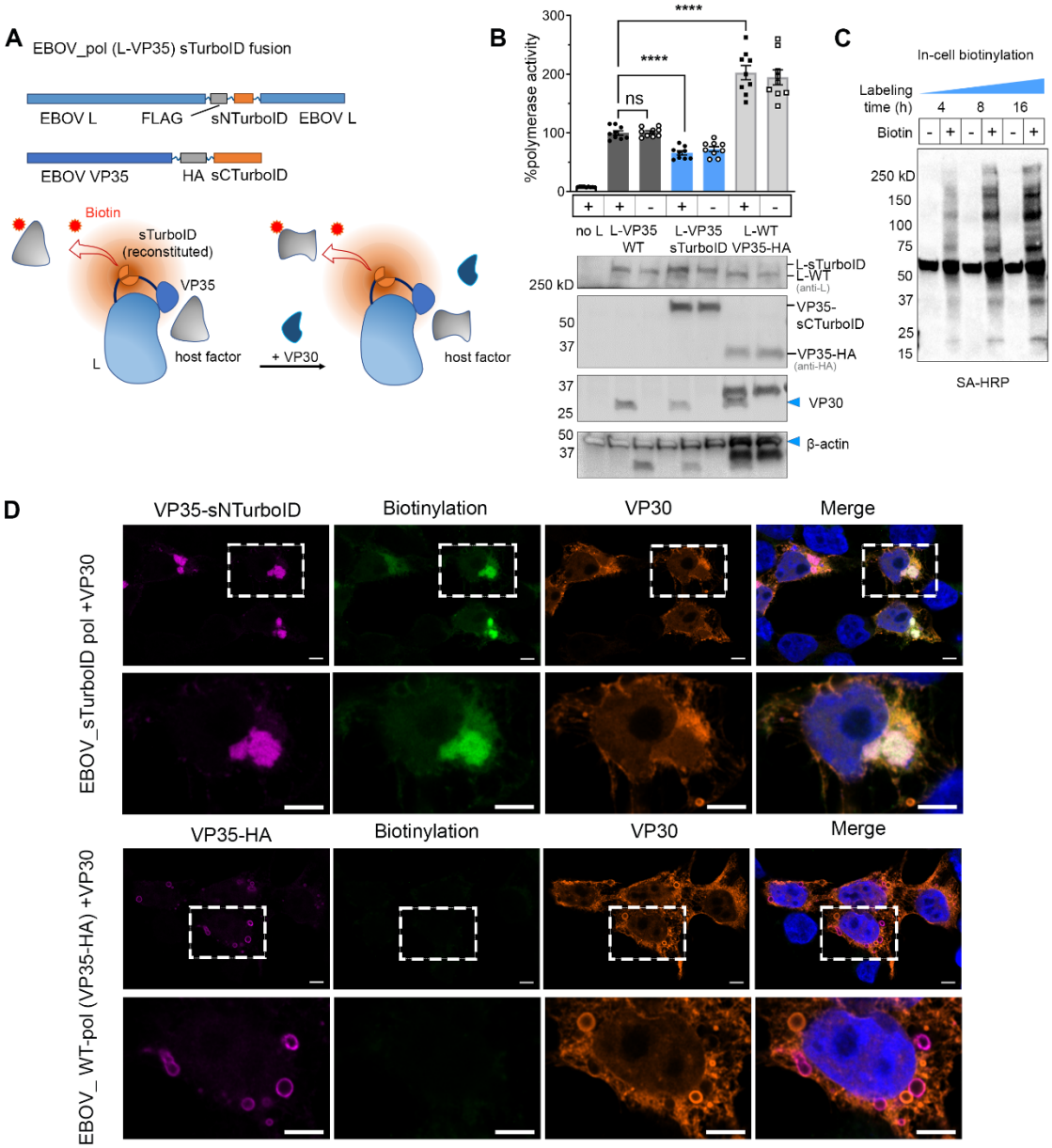

585

586 **Figure 1. Generating a functional EBOV polymerase with proximity-labeling activity.**

587 **(A)** Schematics for proximity biotinylation mediated by the EBOV polymerase (EBOV_pol) split-
588 TurboID fusion in the presence or absence of VP30. **(B)** Polymerase activity and expression of
589 EBOV_pol split-TurboID fusion (L-VP35 sTurboID) compared to controls (L-VP35 WT and L-WT
590 VP35-HA) measured in EBOV minigenome (MG) assay. The percentage of polymerase activity is
591 determined by normalizing luciferase activity in each sample to that of L-VP35 WT control.

592 Background of MG activity is controlled by withdrawing L from the MG system (no L). Results from
593 three independent experiments with triplicate samples were analyzed by using unpaired, two-tailed
594 t test under each condition compared to controls (ns, not significant; *, $p < 0.05$; **, $p < 0.01$; ***, p
595 < 0.001). Values are means ± SEM. Representative western blot showing expression of EBOV L-
596 variants, VP35-variants, VP30 and β-actin in HEK 293T lysates. The blot was sliced into two parts
597 to sequentially probe for different target proteins. **(C)** Streptavidin blot demonstrating biotin ligase
598 activity of EBOV_pol split-TurboID fusion in the context of the EBOV MG system. **(D)** Confocal
599 immunofluorescence images of EBOV_pol split-TurboID mediated proximity biotinylation in cells
600 co-expressing the EBOV MG system. V35-HA and VP35-sNTurboID were all detected by anti-HA.
601 EBOV VP30 was detected by anti-VP30. Biotinylated proteins were detected by streptavidin-
602 AF488. Scale bar: 5 μm. Representative images from two independent experiments. Zoomed
603 region of interest is outlined with a white rectangle in the original image. See also Figure S1 and
604 S2.

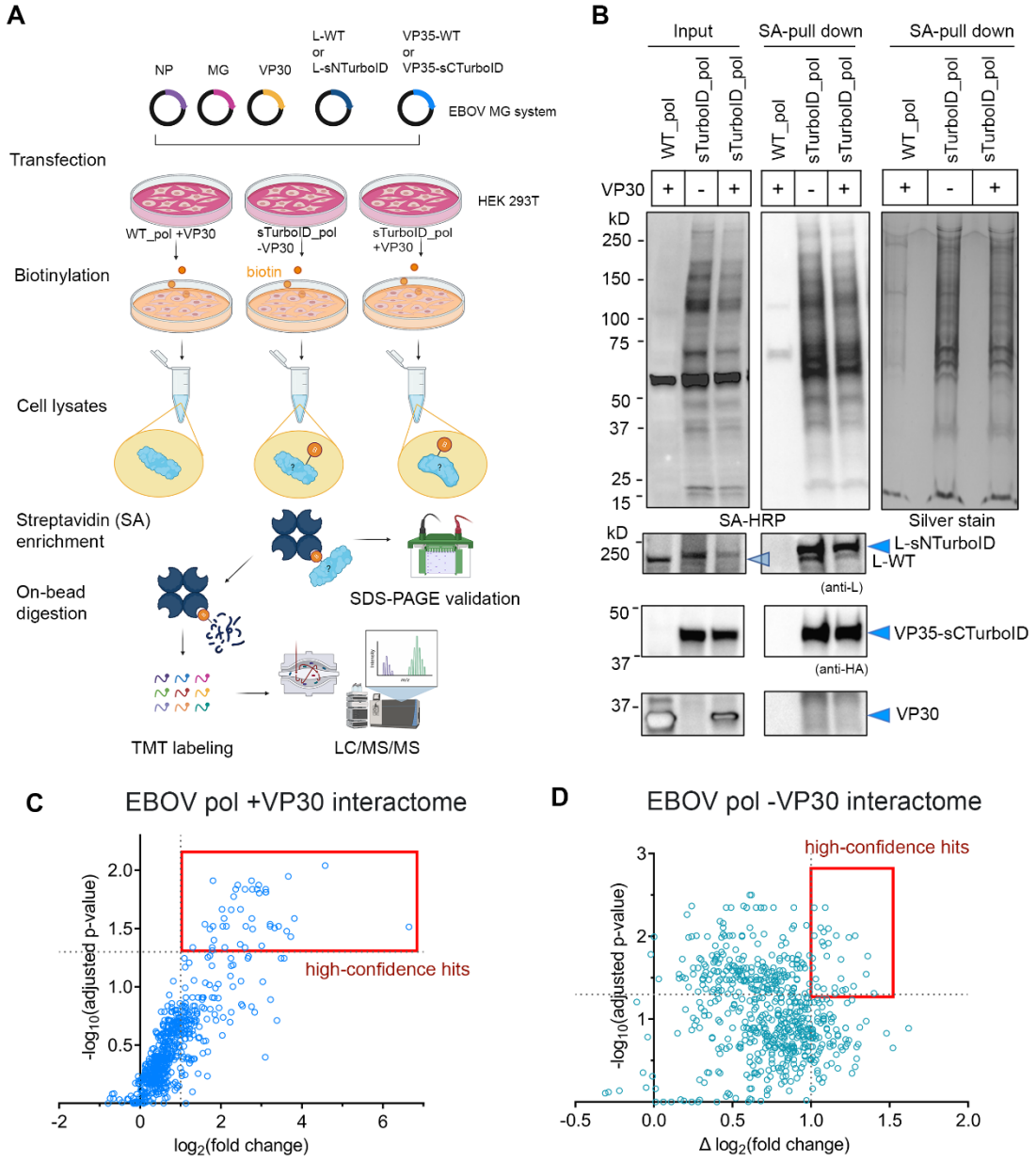

605

606 **Figure 2. Proximity proteomics to define the EBOV polymerase interactomes.**

607 **(A)** Proximity proteomic sample preparation workflow. **(B)** Validation of streptavidin (SA)
608 enrichment of EBOV_pol split-TurboID (sTurboID_pol) mediated proximity biotinylation. Total
609 lysates are indicated as "Input", biotinylated proteins enriched by SA-beads are indicated as "SA-
610 pull down". Representative blots and gels from three biological replicates are shown. All samples
611 were split into three parts that were loaded onto individual gels that were used for streptavidin-HRP
612 blot, to probe EBOV proteins, and for silver staining. The blot used to probe EBOV proteins was

613 sliced into three parts that were imaged separately. Scatter plots showing EBOV polymerase **(C)**
614 and EBOV polymerase differential interacting proteins **(D)** in HEK 293T cells. The degree of
615 enrichment for individual proteins is indicated by fold-change and statistical confidence of
616 enrichment, indicated with an adjusted *p-value*, was calculated and log-transformed. See also
617 Table S1.

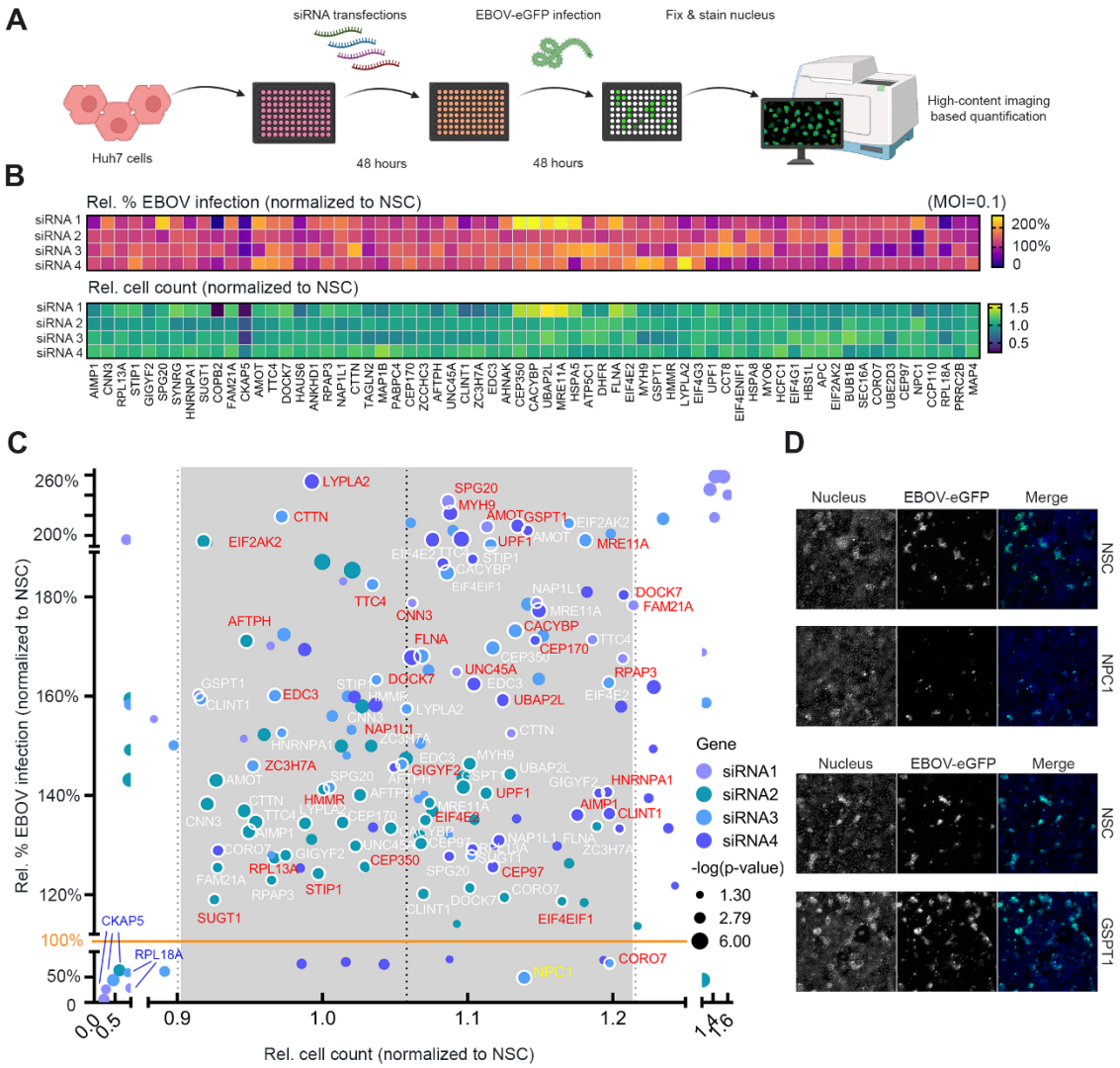

618

619 **Figure 3. Effect of siRNA targeting high-confidence EBOV polymerase interactors on viral**
620 **infection. (A)** Workflow of siRNA screen with authentic EBOV infection. **(B)** Normalized values are
621 displayed in heat maps of relative percentage of EBOV infection and relative cell count. Each value
622 is the mean of technical triplicates. Multiple unpaired t-tests were performed to determine the
623 statistical significance of siRNA-mediated changes on percentage of infection compared to that of
624 NSC. The determined *p-values* were log-transformed and those having *p-value* >0.05 were

625 excluded. **(C)**. Individual genes for which siRNAs significantly affected infection are shown as data
626 points in a bubble plot; data point colors and sizes correspond to the siRNA tested and log-
627 transformed *p-value*, respectively. Data points with multiple siRNAs significantly modulating EBOV
628 infection are considered as true hits and are outlined in white with the corresponding gene also
629 labeled in white. One label of each true hit is shown in red for display purposes. NPC1 used as a
630 positive control is labeled in yellow. **(D)** Representative images of selected Huh7 monolayers at 48
631 hours post-infection. One representative result from two rounds of siRNA screens using different
632 MOIs is shown. See also Figure S3 and S4.

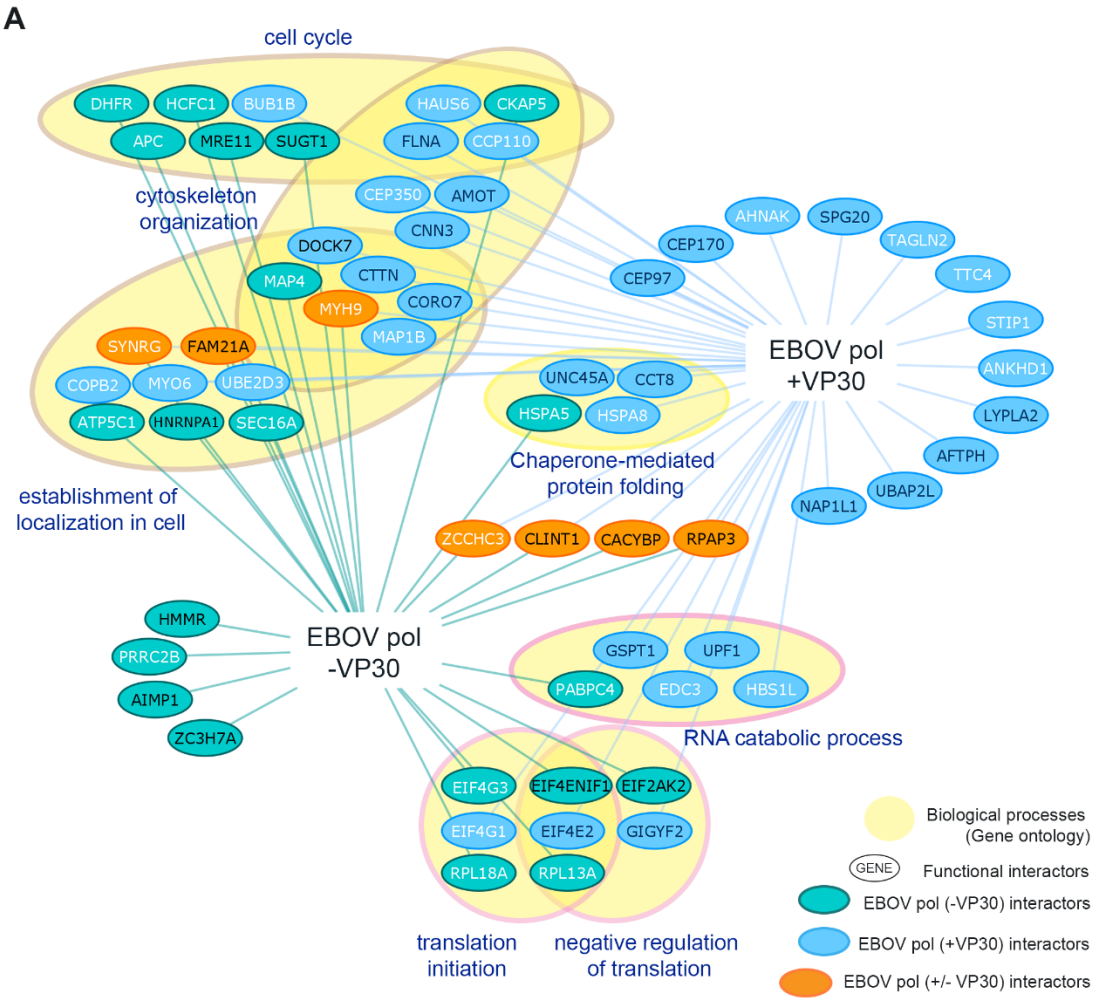
A
cell cycle
DHFR
HCFC1
BUB1B
APC
MRE11
SUGT1
HAUS6
CKAP5
FLNA
CCP110
cytoskeleton organization
CEP350
AMOT
CNN3
DOCK7
MAP4
CTTN
MYH9
CORO7
MAP1B
SYNRG
FAM21A
COPB2
MYO6
UBE2D3
ATP5C1
HNRNPA1
SEC16A
establishment of localization in cell
AHNAK
SPG20
CEP170
TAGLN2
CEP97
TTC4
STIP1
EBOV pol +VP30
ANKHD1
LYPLA2
AFTPH
UBAP2L
NAP1L1
UNC45A
CCT8
HSPA5
HSPA8
Chaperone-mediated protein folding
ZCCHC3
CLINT1
CACYBP
RPAP3
HMMR
PRRC2B
AIMP1
ZC3H7A
EBOV pol -VP30
GSPT1
UPF1
PABPC4
EDC3
HBS1L
RNA catabolic process
EIF4G3
EIF4ENIF1
EIF2AK2
EIF4G1
EIF4E2
GIGYF2
RPL18A
RPL13A
translation initiation
negative regulation of translation
Biological processes (Gene ontology)
GENE
Functional interactors
EBOV pol (-VP30) interactors
EBOV pol (+VP30) interactors
EBOV pol (+/- VP30) interactors

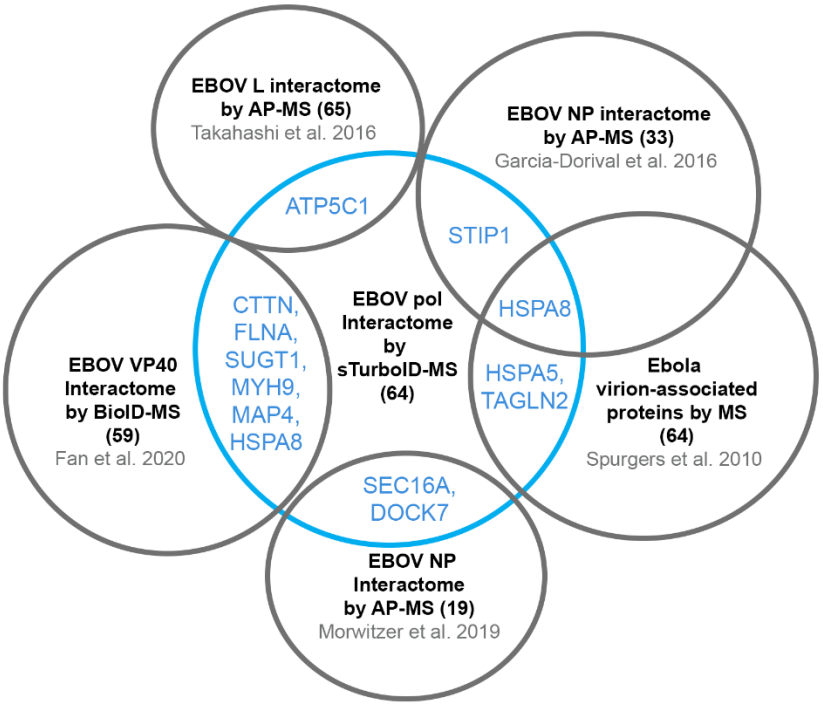
B
EBOV L interactome by AP-MS (65)
Takahashi et al. 2016
EBOV NP interactome by AP-MS (33)
Garcia-Dorival et al. 2016
ATP5C1
STIP1
CTTN, FLNA, SUGT1, MYH9, MAP4, HSPA8
EBOV pol Interactome by sTurboID-MS (64)
HSPA8
HSPA5, TAGLN2
EBOV VP40 Interactome by BioID-MS (59)
Fan et al. 2020
Ebola virion-associated proteins by MS (64)
Spurgers et al. 2010
SEC16A, DOCK7
EBOV NP Interactome by AP-MS (19)
Morwitzer et al. 2019

633

634 **Figure 4. Proximity interactomes of EBOV polymerase in the presence and absence of EBOV**
635 **VP30. (A)** EBOV polymerase interactomes identified by proximity proteomics. Node: high-
636 confidence proteomic hit. Edge: identified protein-protein interaction. Nodes having two edges are
637 shared by multiple interactomes. Black text inside nodes denotes genes that are functionally
638 validated by siRNA screens. Selected nodes are clustered based on enriched biological processes
639 using STRING. **(B)** A Venn diagram comparing EBOV polymerase interactors with reported
640 interactors of EBOV proteins or virions.

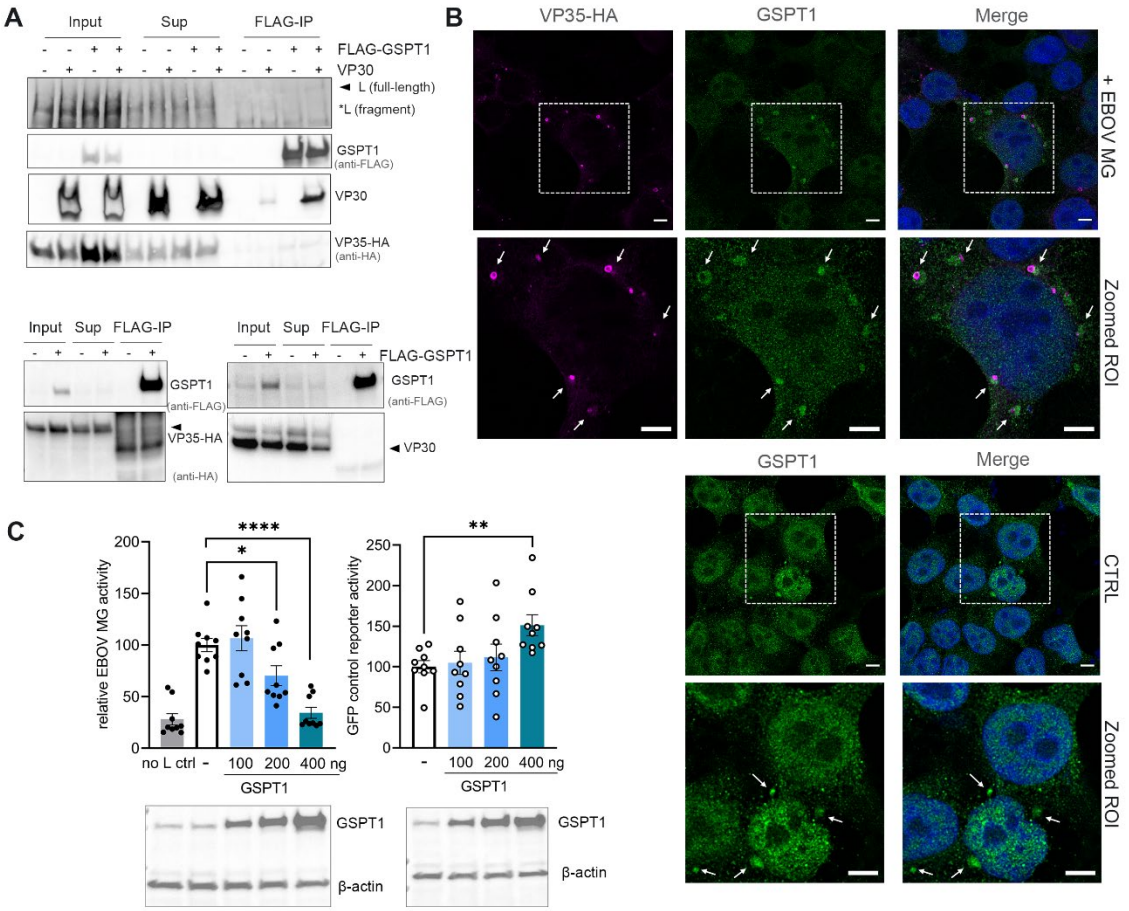

641

642 **Figure 5. GSPT1 is functionally relevant to EBOV RNA synthesis. (A)** co-IP analysis on EBOV
643 polymerase, the accessory proteins (VP30 and VP35) and FLAG-GSPT1. Representative results
644 from three experiments are shown. Each blot was sliced into several parts to probe for different
645 target proteins and imaged separately. **(B)** Confocal immuno-fluorescent analysis of GSPT1 and
646 EBOV_pol (by VP35-HA) localization in the context of the EBOV MG system in HEK 293T cells.
647 Arrowhead: sites where endogenous GSPT1 localize next to viral proteins. The bottom panel shows
648 the subcellular distribution of GSPT1 alone as a negative control. Representative images from two
649 experiments were shown. **(C)** Relative EBOV MG activity and a control GFP reporter activity in

HEK 293T cells overexpressing GSPT1. MG and reporter activity of the GSPT1-overexpressing cells are normalized to that of cells transfected with a control plasmid. Raw luciferase activities and GFP intensities were first normalized to the corresponding amount of total protein in each sample to account for loading bias. Results from three independent experiments with triplicate samples were analyzed by using unpaired, two-tailed t test under each condition compared to controls (*, $p < 0.05$; **, $p < 0.01$; ***, $p < 0.001$, **** $p<0.0001$). Values are means ± SEM. Representative western blot showing the expression level of GSPT1 (long isoform) in different experimental conditions. See also Figure S5.

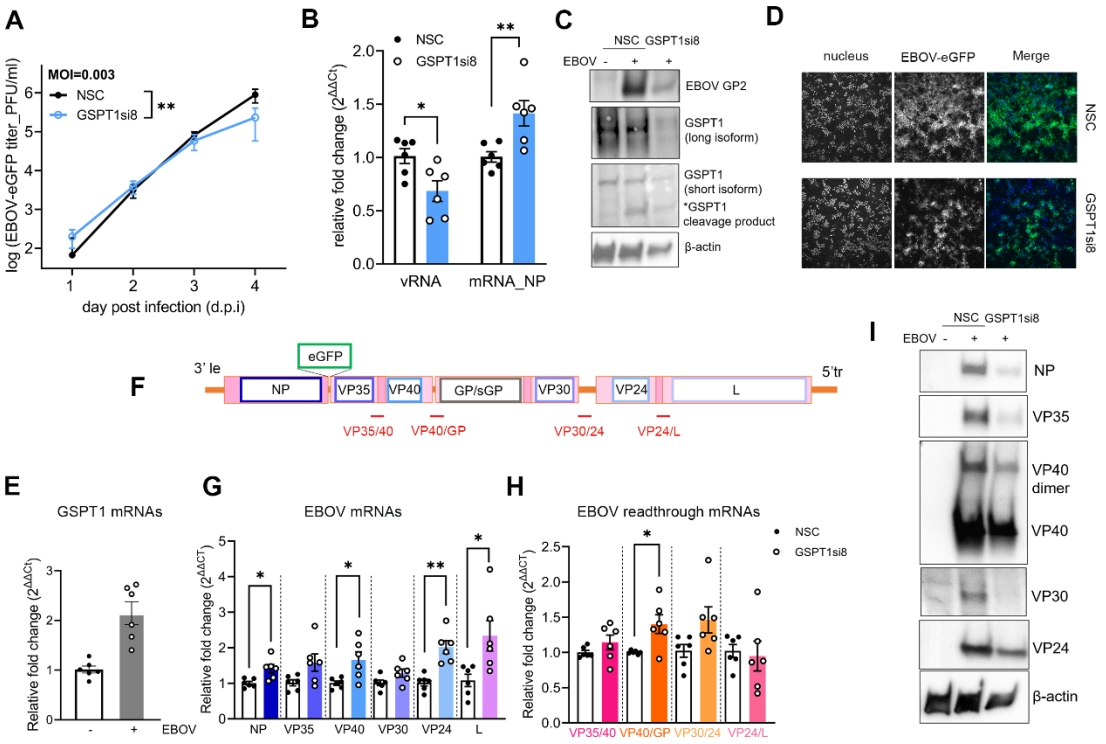

Figure 6. EBOV can subvert GSPT1-restriction and hijack GSPT1 to facilitate viral transcription termination. (A) Effect of GSPT1-KD on the EBOV viral growth kinetics in Huh7 cells. Results of two independent experiments with technical triplicates are plotted as mean ± SD. Two-way ANOVA analysis of log-transformed viral titers was performed to determine the statistical significance of the effect of GSPT1 depletion on viral growth kinetics. **(B)** Effect of GSPT1-KD on EBOV vRNA and NP mRNA accumulation at 4 days post-infection (dpi). **(C)** Western blot analysis of GSPT1 protein and EBOV GP2 levels in lysates from EBOV-infected Huh7 cells harvested at 4 dpi. Representative blots from one experiment are shown. Equal volumes of inactivated lysate were loaded onto two gels to probe cellular or viral proteins separately due to differences in expression levels. **(D)** Representative images of EBOV-infected Huh7 monolayer at 4 dpi are shown. **(E)** Effect

669 of EBOV infection on endogenous GSPT1 expression in Huh7 cells, compared to no infection. **(F)**
670 Schematic of the EBOV-eGFP genome used in the viral growth kinetics experiment. Orange bars:
671 non-coding terminus and intergenic regions. Pink box: gene unit with the coding sequence outlined
672 in a different color. **(G)** Effect of GSPT1-KD on individual EBOV mRNA accumulation. The same
673 data for EBOV NP mRNA levels in GSPT1-depleted cells are as shown in (B), and repeated here
674 to allow comparison with other EBOV mRNAs. **(H)** Effect of GSPT1-KD on the accumulation of
675 EBOV readthrough mRNAs. Locations of each readthrough sequence on the viral genome are
676 marked as red bars in (F). For all bar graphs, results from two independent experiments with
677 triplicate samples were analyzed by using unpaired, two-tailed t test under each condition
678 compared to controls (*, $p < 0.05$; **, $p< 0.01$). Values are means ± SEM. **(I)** Western blot analysis
679 of the effect of GSPT1-KD on accumulations of individual EBOV proteins in Huh7 cells. The same
680 lysates as shown in (C) were used. Equal volumes of inactivated lysate were loaded onto three
681 gels to probe different target proteins. Due to the low expression level of L protein, we could not
682 detect full-length L in inactivated lysate. See also Figure S6.

683

684 **STAR METHODs**

685 **KEY RESOURCES TABLE**

REAGENT or RESOURCE	SOURCE	IDENTIFIER
Antibodies		
Streptavidin-HRP	Thermofisher, Invitrogen	Cat#SA10001
Mouse, anti-HA, 16B12 (monoclonal)	Biolegend Cat#901513	Cat#901513
Human, anti-EBOV NP, KZ51 (monoclonal)	Absolute antibody	Cat#Ab00692-10.0
Rabbit, anti-VP30 (#1-1)	A kind gift from Peter Halfmann and Yoshihiro Kawaoka	N/A
Mouse, anti-EBOV VP24_21.5.2.5 (monoclonal)	A kind gift from Peter Halfmann and Yoshihiro Kawaoka	N/A
Mouse, anti-EBOV VP40	Customized antibody by Zalgen labs/ Autoimmune technology	N/A
Human, BDBV223 (Cross-reactive) Anti-EBOV GP2	A kind gift from James E. Crowe (Flyak et al., 2018)	N/A
Rabbit, polyclonal anti-EBOV L	IBT Bioservices	Cat#0301-045
Rabbit, polyclonal anti-GSPT1/eRF3	Abcam	Cat#ab49878
Streptavidin-AlexaFluor488	Thermofisher/Invitrogen	Cat#s11223
Goat, anti-mouse-HRP	Thermofisher/Invitrogen	Cat#31437
Goat, anti-rabbit-HRP	Southern Biotech	Cat#4050-05
Goat, anti-human-HRP	Thermofisher/Invitrogen	Cat#A18811
Goat, anti-mouse-AlexaFluor568	Thermofisher/Invitrogen	Cat#A11004
Goat, anti-mouse-AlexaFluor647	Thermofisher/Invitrogen	Cat#A21236
Goat, anti-rabbit-AlexaFluor488	Thermofisher/Invitrogen	Cat#A11008
Goat, anti-rabbit-AlexaFluor647	Thermofisher/Invitrogen	Cat#A27040

Streptavidin-magnetic beads	ThermoFisher	Cat#88817
Anti-FLAG M2 affinity Gel	Sigma-Aldrich	Cat#A2220-5ML
Bacterial and virus strains		
EBOV-eGFP (stain Mayinga)	Bukreyev Lab	Initially provided by Jonathan Towner (CDC) and Stuart Nichol (CDC) (Towner et al., 2005)
Chemicals, peptides, and recombinant proteins		
Biotin	Sigma-Aldrich	Cat#B4501
Lipofectamine™ RNAiMAX Transfection Reagent	ThermoFisher/Invitrogen	Cat#13778150
TransIT®-LT1 Transfection Reagent	Mirus	Cat#MIR2306
Sequencing Grade Modified Trypsin	Promega	Cat#V5111
NEBBuilder HiFi DNA Assembly Master Mix	NEB	
In-Fusion® HD Cloning Plus	Takara	Cat# 638920
16% Paraformaldehyde Aqueous Solution, EM Grade, Ampoule 10ML	Electron Microscopy Sciences	Cat#15710
ProLong™ Gold Antifade Mountant	ThermoFisher/Invitrogen	Cat#P36934
Normal Goat Serum	ThermoFisher/Invitrogen	Cat#PCN5000
Hoechst 33342, Trihydrochloride, Trihydrate, 100 mg	ThermoFisher/Invitrogen	Cat#H1399
RIPA Buffer (10X)	Cell Signaling Technology	Cat#9806S
cOmplete™, EDTA-free Protease Inhibitor Cocktail	Roche	SKU# 11873580001
Benzonase® Nuclease, Purity > 90%	Millipore/Sigma	Cat#70746
NuPage Sample reducing agent (10X)	ThermoFisher	Cat#NP0009
NuPage LDS sample buffer (4X) (Laemmli)	ThermoFisher	Cat#NP0008

TRIzol™ Reagent	ThermoFisher/Invitrogen	Cat# 15596018
DEPC-Treated Water	ThermoFisher/Invitrogen	Cat#AM9920
Iodoacetamide (IAA)	Sigma-Aldrich	SKU#I1149-5G
Critical commercial assays		
Pierce™ BCA Protein Assay Kit	Thermo Scientific	Cat#23225
Pierce™ Silver Stain for Mass Spectrometry	Thermo Scientific	Cat#24600
SuperSignal™ West Pico PLUS Chemiluminescent Substrate	Thermo Scientific	Cat#34578
Luciferase Assay System	Promega	Cat#E4550
CellTiter-Glo® 2.0 Cell Viability Assay	Promega	Cat#G9241
High-Capacity cDNA Reverse Transcription Kit with RNase Inhibitor	ThermoFisher scientific (Applied Biosystems)	Cat#4374966
SYBR™ Select Master Mix	ThermoFisher scientific (Applied Biosystems)	Cat#4472908
Direct-zol RNA Miniprep Plus	Zymo research	Cat#R2071
ZipTip with 0.2 µL C18 resin	Millipore	Cat# ZTC18M096
TMT10plex™ Isobaric Label Reagent Set, 1 x 0.8 mg	Thermo Scientific	Cat# 90110
Deposited data		
Raw proximity proteomic data of EBOV polymerase interactome	This study	Table S1
Experimental models: Cell lines		
HEK 293T	ATCC	Cat#CRL-3216
VERO C1008 [Vero 76, clone E6, Vero E6]	ATCC	Cat# CRL-1586
Huh7 used in BSL4	A kind gift from Mariano Garcia-Blanco	

Huh7 used in BSL2	A kind gift from Luke Wiseman	
Oligonucleotides		
Primers for RT-qPCRs, see Table S2	This paper	N/A
siRNAs for knockdowns, see Table S3	This paper	N/A
AllStars Negative Control siRNA	Qiagen	Cat#1027281
Oligo dT(20) Primer	Thermofisher/invitrogen	Cat#18418020
Recombinant DNA		
Plasmid: pCEZ-NP	(Jasenosky et al., 2010b)	N/A
Plasmid: pCEZ-VP35	(Jasenosky et al., 2010b)	N/A
Plasmid: pCDNA5-VP35-HA	(Fang et al., 2018)	N/A
Plasmid: pCAGGS-VP35-HA	This study	N/A
Plasmid: pCAGGS-VP35-sNTurboID	This study	N/A
Plasmid: pCEZ-VP30	(Jasenosky et al., 2010b)	N/A
Plasmid: pCEZ-L	(Jasenosky et al., 2010b)	N/A
Plasmid: pCEZ-L-sCTurboID	This study	N/A
Plasmid: pHH21-3E5E-Fluc	(Jasenosky et al., 2010b)	N/A
Plasmid: pCI-empty	This study	N/A
Plasmid: pCI-MS2V5-eRF3a F76a	(Fatscher et al., 2014)	Plasmid #65811
Plasmid: pCI-FLAG-GSPT1	This study	N/A
Plasmid: pCAGGS-eGFP	This study	N/A
Plasmid: pCAGGS-empty	This study	N/A
Plasmid: pLX304 CMV HA-HaloTag-FRB-sTurboID (C)	(Cho et al., 2020)	Plasmid: #153003

Plasmid: pLX304 CMV FKBP-V5-sTurboID (N)	(Cho et al., 2020)	Plasmid: #153002
Plasmid: pFastBac™ Dual Expression Vector	ThermoFisher/Gibco	Cat#10712024
Software and algorithms		
GraphPad Prism 9	GraphPad	N/A
Cytoscape v3.8.2	Cytoscape	https://cytoscape.org/
Image Lab Software	Bio-Rad	https://www.bio-rad.com/en-us/product/image-lab-software
SparkControl™	Tecan	
BioRender	BioRender	https://biorender.com/
Thermo Scientific™ HCS Studio Cell Analysis Software	Thermo Scientific	CX51110
ZEISS ZEN 3.4 Blue edition	ZEISS	https://www.zeiss.com/
FIJI	(Schindelin et al., 2012)	https://imagej.net/software/fiji/
ImageJ	(Schneider et al., 2012)	https://imagej.nih.gov/ij/
SnapGene Viewer	SnapGene	https://www.snapgene.com/snapgene-viewer/
STRING	(Szklarczyk et al., 2019)	https://string-db.org/
Proteome Discover v 2.3	Thermo Scientific	
SEQUEST	Yates Laboratory	http://proteomicswiki.com/wiki/index.php/SEQUEST
Scaffold 4	Proteome Software	

686

687 **Resource availability**

688 **Lead contact**

689 Further information and requests for resources and reagents should be directed to and will be
690 fulfilled by the Lead Contact, Erica Ollmann Saphire (erica@lji.org).

691 **Materials availability**

692 All requests for unique reagents generated in this study should be directed to and will be fulfilled
693 by the Lead Contact author. Materials will be made available through the authors upon execution
694 of a Material Transfer Agreement.

695 **Data and code availability**

696 Raw proteomic data reported in this study are reported in Table S1.

697 **Experimental model and subject details**

698 **Cell cultures**

699 Human hepatocytes Huh7 and human embryonic kidney cells HEK 293T were maintained in
700 Dulbecco's modified Eagle medium (DMEM-GlutaMAX) supplemented with 4.5 g/L D-Glucose,
701 10% fetal bovine serum (FBS), penicillin (100 U/ml), streptomycin (100 µg/ml). For cells used in
702 viral infection experiment, Huh7 were cultured in Dulbecco's modified Eagle medium (DMEM)
703 supplemented with 10% FBS and 50 µg/ml Gentamicin Sulfate; Vero-E6 cells were cultured in
704 Minimum Essential Medium (MEM) supplemented with 10% FBS, 1% MEM Non-essential Amino
705 Acid Solution, 1% Sodium pyruvate solution, and 50 µg/ml Gentamicin Sulfate. All cells were grown
706 at 37°C and 5% CO2.

707 **Virus stock**

708 EBOV strain Mayinga expressing Emerald green fluorescent protein (eGFP) (1) was propagated in
709 Vero-E6 cells with 500,000 plaque-forming unit (PFU) per T225 flask (at 90% confluency). EBOV-
710 eGFP was harvested 5 days post-infection. All experiments using infectious EBOV were performed
711 under biosafety level 4 (BSL-4) conditions at the Galveston National Laboratory. Virus inactivation
712 was performed according to standard operating procedures.

713 **METHOD DETAILS**

714 **Plasmids and cloning**

715 To generate pCEZ-L-sCTurboID, a fragment of L coding sequence was first subcloned into a
716 pFastbacDual intermediate plasmid using the natural restriction sites Pac1 and Hpa1. From there,
717 a fragment of sequence encoding the sC-TurboID and a FLAG-tag sequence, flanked by two
718 flexible linkers was internally inserted at the position 1705/1706 (TTIP/Q). This insertion was PCR
719 amplified from pLX304 CMV HA-HaloTag-FRB-sTurboID (C), and inserted to the intermediate
720 plasmid using NEBuilder HiFi DNA Assembly Master Mix (NEB). The L-sNTurboID fragment was
721 ligated back to the pCEZ-L backbone using the same restriction sites Pac1 and Hpa1 by NEB T4
722 ligase.

723 To generate pCAGGS-VP35-HA, the coding sequence of VP35-HA was subcloned to the plasmid
724 pCAGGS-empty using the restriction sites Kpn1 and Xho1 by standard ligation method. To
725 generate pCAGGS-VP35-sNTurboID, pcDNA5-VP35-HA (gift from Mariano Garcia-Blanco) was
726 linearized. The fragment of sNTurboID was PCR amplified from pLX304 CMV FKBP-V5-sTurboID
727 (N) and cloned into the pcDNA5-VP35-HA using NEBuilder HiFi DNA Assembly Master Mix (NEB).
728 The fragment of VP35-sNTurboID, including the C-terminal HA tag, was subcloned to pCAGGS
729 plasmid using restriction sites Kpn1 and Nhe1 and standard ligation method.

730 To generate pCI-empty, the coding sequence of MS2V5-eRF3a-F76a was removed from pCI-
731 MS2V5-eRF3a F76a plasmid (a gift from Niels Gebring) by PCR and re-circularized using
732 NEBuilder HiFi DNA Assembly Master Mix (NEB). To generate pCI-FLAG-GSPT1, the coding
733 sequence of MS2V5 was removed from pCI-MS2V5-eRF3a F76a plasmid and an N-terminal FLAG
734 tag was inserted to the same plasmid by PCR and re-circularized using NEBuilder HiFi DNA
735 Assembly Master Mix (NEB). The F76a mutation was mutated back to wildtype using In-fusion
736 cloning (Clontech).

737 The sequence of all engineered plasmid DNA was confirmed by Sanger sequencing.

738 **EBOV minigenome assay**

739 HEK 293T cells (2×10^5 per well) were seeded in 24-well plates one day prior to transfection with
740 the following plasmids: 100 ng pCEZ-NP, 100 ng pCEZ-VP35, 75 ng pCEZ-VP30, 750 ng pCEZ-L,
741 62.5 ng EBOV minigenome encoding a firefly luciferase reporter (pEE21). In some cases: pCEZ-
742 VP30 was replaced with equal mass of control pCAGGS-empty plasmid; pCEZ-L and/or pCEZ-
743 VP35 were replaced with a tagged variant. A negative control was included in every assay in which
744 the pCEZ-L plasmid was replaced with equal mass of control pCAGGS-empty plasmid to verify
745 minigenome activity mediated by EBOV polymerase. Plasmids were transfected with TransIT-LT1
746 transfection reagent (3 µl/µg plasmid). At 48 hours post-transfection, cells were lysed and subjected
747 to the luciferase reporter assay (Promega).

748 To measure the effect of GSPT1 knockdown on EBOV minigenome activity, we modified the assay
749 as below. HEK 293T cells (1×10^5 per well) were seeded in 24-well plates one day prior to siRNA
750 or plasmid. To knockdown GSPT1, cells were transfected with 10 nM of the siRNA, GSPT1si8,
751 using Lipofectamine RNAiMAX. In control wells, cells were transfected with 10 nM of the Allstar
752 negative control siRNA (NSC) using Lipofectamine RNAiMAX. To overexpress GSPT1, cells were
753 transfected with 100/200/400 ng of pCI-FLAG-GSPT1 (per well) using TransIT-LT1. In control wells,
754 cells were transfected with 200 ng of pCI-empty control vector using TransIT-LT1. At 24 hours post-
755 transfection, cells were transfected with the EBOV MG system described earlier. In the control

756 plate, cells were transfected with 100 ng of pCAGGS-eGFP (per well) using TransIT-LT1 to
757 evaluate the effect of GSPT1 modulation on a control reporter expression. Two days after the
758 second transfection, cell lysate was harvested in 1X passive lysis buffer for luciferase reporter
759 assay or in GFP lysis buffer (50mM Tris pH7.4, 1mM EDTA, 0.5% NP-40, 150mM NaCl) to quantify
760 the fluorescence intensity. A fraction of each lysate was used to quantify the total protein by BCA
761 assay. Raw luciferase intensity or GFP intensity of each sample was first normalized to the BCA
762 quantified protein amount. The resulting relative luciferase reporter activity or GFP reporter activity
763 was further normalized to that of the control: NSC for the GSPT1 knockdown experiment, pCI-
764 empty for the GSPT1 overexpression experiment.

765 **Biotinylation with polymerase-TurboID fusion protein**

766 HEK 293T cells seeded in 24-well plates were transfected with EBOV minigenome system including
767 the wild-type polymerase or the polymerase-TurboID fusion. Biotin (500 μM) was added to cell
768 culture media 2-3 days post-transfection. Multiple labeling time points were sampled for
769 optimization. The reaction was stopped by placing cells on ice, the excess biotin was removed by
770 DPBS washes, and soluble whole cell lysates were collected for western blot analysis using
771 streptavidin-HRP.

772 **Immunofluorescent analysis (IFA) using confocal microscopy:** Acetone cleaned, glass
773 coverslips (1.5 mm thickness) placed inside 24-wells were treated with human fibronectin (50
774 mg/ml) for 20 min at 37 ℃ incubator, prior to HEK 293T cells seeding ($4X10^4$/well). Twenty-four
775 hours later, the monolayer was transfected with the EBOV minigenome system using Trans-IT LT1
776 as described earlier. For in-cell biotinylation experiment: at the same day of transfection, biotin (500
777 μM) was added to the culture media allowing for 18 hours in-cell biotinylation in EBOV minigenome
778 transfected cells. Labeling was stopped by washing cells with cold DPBS for three times. For all
779 IFA specimens, cells were fixed in 4% paraformaldehyde for 15 mins, quenched with 20mM
780 Glycine-DPBS for 5 mins, permeabilized with 0.1% Triton-X100-DPBS for 10 mins, and blocked in
781 1% normal goat serum for at least one hour, all at room temperature. Primary antibody incubations
782 were performed at room temperature for two hours or at 4 ℃ overnight. Specimens were washed
783 three times with PBS-0.1% Tween-20 and incubated with secondary antibodies for one hour at
784 room temperature. Nuclei were counterstained by Hoechst. Confocal images were acquired on
785 Zeiss LSM880-airyscan system under super-resolution mode, using a 63x/NA1.4 oil objective.

786 For samples shown in the Figure 1D, mouse anti-HA (1:500) and rabbit anti-VP30 (1:500) antibody
787 were used as the primary antibodies, goat anti-mouse AlexaFluor647 (1:500) and goat anti-rabbit
788 AlexaFluor 568 (1:500) were used as the secondary antibodies. Together these combinations were

789 used to probe HA-tagged EBOV VP35 (VP35-HA and VP35-sNTurboID) and the wildtype VP30.
790 Streptavidin-AlexaFluor488 (1:500) was added along with secondary antibodies to probe
791 biotinylated proteins.

792 For samples shown in Figure 5B, mouse anti-HA (1:500) and rabbit anti-GSPT1 (1:500) antibody
793 were used as the primary antibodies, goat anti-mouse AlexaFluor568 (1:500)and goat anti-rabbit
794 AlexaFluor 488 (1:500) were used as the secondary antibodies. Together these combinations were
795 used to probe EBOV VP35-HA and the endogenous GSPT1 protein.

796 **Sample preparation for in-cell biotinylation and streptavidin enrichment**

797 Protocol adapted from a previous study (Branon et al., 2018). HEK 293T cells were seeded in 6-
798 wells plate ($1X10^6$ cells per well) and transiently transfected using Trans-IT LT1 a day after, with
799 EBOV MG plasmids including plasmid expressing wild-type or the TurboID-fused viral polymerase.
800 To enable in-cell biotinylation, at two days post-transfection, monolayers expressing EBOV MG are
801 incubated with 500 µM biotin containing complete media for indicated times. Biotinlyation was
802 stopped by washing monolayers with cold DPBS twice before collecting the cell pellets by
803 centrifugation at 1500 rpm for 3 mins at 4 ºC. Cell pellets (1V) were lysed in 1V of 1X RIPA buffer
804 containing cOmplete™, EDTA-free Protease Inhibitor Cocktail (Roche) and Benzonase® Nuclease
805 (Millipore) followed by incubation on ice for 15-20 mins. Soluble lysates were clarified by
806 centrifugation at 13000 rpm for 5 mins at 4 ºC.

807 For streptavidin enrichment, streptavidin-magnetic beads (80 µl slurry/mg of total protein) were
808 washed with 1X RIPA buffer twice and incubated with 2-3 mg of soluble cell lysate for one hour at
809 room temperature. The beads were subsequently washed twice with 1 ml of 1X RIPA buffer, once
810 with 1 ml of 1M KCL, once with 1 ml of 0.1M Na_2CO_3, once with 1 ml of 2M Urea in 10 mM Tris-
811 HCl (pH 8.0), and with twice with 1 ml 1X RIPA buffer. Washed beads were then either eluted in
812 50 uls of NuPage LDS sample buffer (4X) supplemented with 20 mM DTT and 2 mM biotin for
813 quality check or processed to on beads digestion. Quality checks for successful streptavidin
814 enrichment include silver staining and western blotting of SDS-PAGE-separated input and
815 streptavidin-enriched samples side-by-side.

816 For on-bead digestion, proteins bound to beads were further washed twice with 50 mM Tris HCL
817 (pH 7.5) and two washes of 2 M urea/50 mM Tris buffer (pH 7.5). A final volume of 80 µl of 2 M
818 urea/50 mM Tris containing 1 mM DTT and 0.4 µg trypsin was added to washed beads for overnight
819 digestion at 37 ºC shaker. Digested supernatants containing biotinylated peptides were transferred
820 to a new tube. The streptavidin beads were washed twice with 60 µl of 2 M urea/50 mM Tris buffer
821 (pH 7.5) and the rests were combined with the on-bead digest supernatant. The eluate was reduced

822 with 4 mM DTT for 30 mins at room temperature with shaking, alkylated with 10 mM IAA
823 (iodoacetamide) for 45 mins in the dark at 25 ºC with shaking. An additional 0.5 µg of trypsin was
824 added to the sample and the digestion was completed overnight at 37 ºC shaker. After final
825 digestion, samples were acidified by adding formic acid to a final concentration of 1 % and stored
826 in - 80 ºC freezer before sending to Scripps Research (FL) Proteomic core for further processing,
827 TMT labeling, and mass-spectrometry analysis.

828 **Proximity proteomics (with tandem-mass-tag labeling):** Following on-bead trypsin digestion of
829 biotinylated proteins, LASSA (WT and TurboID) and EBOLA (WT, TurboID MINUS and TurboID
830 PLUS) samples were acidified by the addition of 1% formic acid and desalted with 2 µg-capacity
831 C18 ZipTips, respectively, and dried using vacuum. Peptides were resuspended in 100mM TEAB
832 and labelled with TMT labels (10-plex, with one TMT label not used) according to the
833 manufacturer's instructions and pooled.

834 The labelling scheme for three biological replicates of each condition was as follows:

EBOLA sample	WT_pol+VP30_01	WT_pol+VP30_02	WT_pol+VP30_03
TMT 10-plexs label	126	127C	128C
EBOLA sample	TurboID_pol-VP30_01	TurboID_pol-VP30_02	TurboID_pol-VP30_03
TMT 10-plexs label	127N	128N	131
EBOLA sample	TurboID_pol+VP30_01	TurboID_pol+VP30_02	TurboID_pol+VP30_03
TMT 10-plexs label	129N	130N	129N

835 The pooled and multiplexed samples were dried under vacuum, re-solubilized in 1% TFA and then
836 desalted using 2 µg-capacity C18 ZipTips (Millipore, Billerica, MA), and then dried once again using
837 vacuum. For mass spectrometry, dried TMT-labelled peptides were reconstituted in 5 µL of 0.1%
838 TFA, vortexed briefly, and then sonicated for 15 mins. The peptides were subsequently on-line
839 eluted into a Fusion Tribrid mass spectrometer (ThermoFisher Scientific, San Jose, CA) from an
840 Acclaim PepMapTM RSLC C18 nano Viper analytical column (2 mm, 100 Å, 75-µm ID × 50 cm,
841 Thermo Scientific, San Jose, CA) using a gradient of 5-25% solvent B (80/20 acetonitrile/water,
842 0.1% formic acid) in 180 mins, followed by 25-44% solvent B in 60 mins, 44-80% solvent B in 0.1
843 min, a 5-mins hold of 80% solvent B, a return to 5% solvent B in 0.1 min, and finally a 20-mins hold
844 of solvent B. All flow rates were 300 nl/min delivered using a nEasy-LC1000 nano liquid
845 chromatography system (Thermo Fisher Scientific, San Jose, CA). Solvent A consisted of water

846 and 0.1% formic acid. Ions were created at 2.1-2.5 kV using the EASY-SprayTM ion source held
847 at 50 ºC (Thermo Fisher Scientific, San Jose, CA). A synchronous precursor selection (SPS)-MS3
848 mass spectrometry method was used based on published protocol (Ting et al., 2011), scanning
849 between 380-2000 m/z at a resolution of 120,000 for MS1 in the Orbitrap mass analyzer, and
850 performing CID at top speed in the linear ion trap of peptide monoisotopic ions with charge 2-8,
851 using a quadrupole isolation of 0.7 m/z and a CID energy of 35%. The top 10 MS2 ions in the ion
852 trap between 400-1200 m/z were then chosen for HCD at 65% energy and detection in the Orbitrap
853 at a resolution of 60,000 and an AGC target of 1E5 and an injection time of 120 msec (MS3). Three
854 technical replicates were performed for each sample.

855 **Bioinformatic analysis of mass spectrometry data:** The raw data technical replicates were
856 added as "fractions" into Proteome Discover v 2.3 (Thermo Fisher Scientific, San Jose, CA). As it
857 is the default option for this software, peptide spectrum match raw values of both technical
858 replicates from the same biological sample were summed for the same peptide group discovery.
859 Quantitative analysis of the TMT experiments was performed simultaneously to protein
860 identification. The precursor and fragment ion mass tolerances were set to 10 ppm, 0.6 Da,
861 respectively), enzyme was Trypsin with a maximum of 2 missed cleavages. Steptavidin FASTA
862 and Uniprot Human proteome FASTA file with added sequences specific for EBOV proteins and
863 TurboID fusion proteins, were used in SEQUEST searches. The impurity correction factors
864 obtained from Thermo Fisher Scientific for each kit was included in the search and
865 quantification. The following settings were used to search the streptavidin enriched data; dynamic
866 modifications; Oxidation / +15.995Da (M), Deamidated / +0.984 Da (N, Q), TMT6plex / +229.163
867 Da (K) ,Biotin / +226.078 Da (K) and static modifications of TMT6plex / +229.163 Da (N-Terminus),
868 Carbamidomethyl +57.021 (C). Only unique+ Razor peptides were considered for quantification
869 purposes. Target Decoy feature of Proteome Discoverer 2.3 was used to set a false discovery rate
870 (FDR) of 0.01. Total peptides quantified were normalized to *Streptavidin* to adjust for loading bias
871 and Protein Abundance Based method was used to calculate the protein level ratios. Low
872 Abundance Resampling method was used to impute missing data and co-isolation threshold and
873 SPS Mass Matches threshold were set to 50 and 65, respectively. ANOVA (Individual Proteins)
874 was performed using Proteome Discoverer 2.3 workflow and FDR of 0.05 was chosen as the cut
875 off to identify the top tier proteins that are differentially expressed across WT and TurboID samples.

876 Sequences added to the Uniprot Human proteome database for this experiment:

877 - Ebola VP30
878 - Ebola NP
879 - Ebola VP35_wildtype

880 - Ebola L_wildtype
881 - Ebola VP35_sCTurboID fusion protein
882 - Ebola L_sNTurboID fusion protein

883 **Thresholding and network analysis of viral polymerase-proximity interactome:** To curate a
884 list of high confident hits for both viral polymerase-proximity interactome, we applied a threshold of
885 > 1 for log_2 transformed relative (rel.) abundance ratio (TurboID_pol/WT_pol) and a threshold of <
886 0.05 for the adjusted *p-value* for each abundance ratio. To analyze the differential interactome of
887 EBOV polymerase with and without VP30, since the experimental set up only included the wild-
888 type EBOV polymerase with VP30 as the control, abundance ratios of proteins identified in the
889 TurboID polymerase interactome with or without VP30 were first normalized to the WT pol +VP30
890 control to get the log_2(fold change) value. Subsequently, the difference of the two log_2(fold change)
891 values, Δlog_2(fold change), was determined as a measure of the differential interactome of EBOV
892 polymerase with and without VP30. To curate a list of high confidence hits , we retained the same
893 threshold of "< 0.05" for the adjusted *p-value* for corresponding abundance ratio of (TurboID_pol -
894 VP30/WT_pol) and further applied a threshold of Δlog_2(fold change) >1. Above mentioned lists
895 including critical parameters used in thresholding were presented in **Table S1**.

896 High-confidence hits in both EBOV polymerase interactomes in the presence and absence of VP30
897 were displayed as protein-protein networks using Cytoscape. The web-based bioinformatic
898 analyzer STRING was used to perform functional enrichment analysis to cluster nodes involved in
899 the same biological process (FDR< 1%).

900 **siRNA screen with authentic EBOV infected cells**

901 Huh7 cells (5 x 10^3 per well) were seeded in clear-bottom, black 96-wells plate, leaving edge wells
902 filled with DPBS. Twenty-four hours, Huh7 monolayers were transfected with 10 nM of individual
903 siRNAs using Lipofectamine RNAiMAX (0.1 ul per well). Knock down (KD) of each target was
904 performed using four individual siRNA transfections, each one performed in triplicate. Each plate
905 includes two sets of triplicated internal control wells transfected with 10 nM AllStar negative control
906 (NSC) to account for plate-to-plate variations. Forty-eight hours later, plates were transferred to
907 BSL4 for infection with EBOV-eGFP at indicated MOIs. Infected monolayers were fixed and
908 inactivated by 10% formalin at two days post-infection and removed from BSL4 facility. Fixed
909 monolayers were stained with Hoechst (1 µg/ml in DPBS) for 15 mins at room temperature prior to
910 imaging. Percentage of EBOV-eGFP infected Huh7 cells (% infection) and cell count with different
911 siRNA treatment were quantified by CellInsight™ CX5 High Content Screening (HCS) Platform
912 (ThermoFisher) using a 10x objective.

913 Relative % virus infection and relative cell count were calculated by normalizing raw percent viral
914 infection rate and cell count of individual siRNA treatment to corresponding control wells in each
915 plate. Heat maps showing relative %virus infection and relative cell count were generated by
916 GraphPad Prism 9 using the normalized value of each individual siRNA treatment. The mean of
917 numerical values from each triplicated well are used for plotting. To quantitatively analyze the
918 impact of siRNA treatment on viral infection and cell count, multiple t-tests were performed,
919 comparing normalized % infection of each siRNA treatment to corresponding NSC control. Bubble
920 plots were generated by plotting numerical values of normalized cell count of each siRNA treatment
921 against their value of normalized % infection if their *p-value* (represented by the size of each data
922 point) was < 0.05. Outliers with cell count significantly different from the average by one standard
923 deviation were ruler out because the effect of siRNA treatment on %infection in these cases can
924 be confounded by a marked alteration in the total number of cells. siRNAs used for the screen were
925 from the Genome-wide ON TARGET-Plus (OTP) Human siRNA library from Dharmacon/Thermo
926 Scientific. Sequence information of each siRNA been used is curated in **Table S2**.

927 **Co-Immunoprecipitations (co-IP)**

928 Co-IP reactions were performed as previously described(Fang et al., 2018). HEK 293T cells
929 ($1X10^6$) were seeded in 6-wells plate. Twenty-four hours later, cells in each well were transfected
930 with 500 ng of pCI-empty or pCI-FLAG-GSPT1 plasmid combined with 3 µg of pCEZ-L and 400 ng
931 of pCAGGS-VP35-HA, plus and minus 300 ng of pCEZ-VP30, using TransIT LT1 transfection
932 reagent. For experiments probing interactions between GSPT1 and EBOV VP35 or VP30, 1 µg of
933 pCI-empty or pCI-FLAG-GSPT1 plasmid combined with 1 µg of pCAGGS-VP35-HA or pCEZ-VP30
934 (per well) were added to the co-transfection mix using the Lipofectamine 3000 transfection reagent.
935 Three days later, transfected cells were washed with DPBS and lysed in 1X RIPA buffer including
936 protease inhibitor cocktail (cOmplete™, EDTA-free Protease Inhibitor Cocktail), on ice for 15 mins.
937 Soluble whole cell lysates were clarified by centrifugation at 12,000X rpm for 10 mins. FLAG-M2
938 affinity beads (40 µl per reaction) were washed with DPBS for once, NT2 buffer for twice before
939 blocking with BSA in NT2 buffer (0.5 mg/ml) for 0.5 – 1 hour at room temperature. Lysates
940 containing equal amounts of total protein (1-1.5 mg determined by BCA assay) were incubated with
941 BSA-blocked FLAG-M2 affinity beads and rotate overnight at 4 ºC. Supernatant containing
942 unbound proteins was removed by spin at 5000x g for 30 s, followed by four washes in 1 ml NT2
943 buffer. Immunoprecipitated proteins were eluted in 4X-SDS-loading buffer containing reducing
944 agent with 10 mins incubation at 95 ºC and analyzed by western blotting.

945 **Viral growth kinetics and quantification of viral proteins and RNAs**

946 Huh7 cells (5×10^4 per well) were seeded in 24-well plates and transfected with 10 nM siRNA (NSC
947 or GSPT1 si8, experimentally validated). Forty-eight hours after transfection, Huh7 monolayers
948 were transferred into BSL-4 facilities and infected with EBOV-eGFP at an MOI of 0.003 (PFU/ml)
949 for one hour. Infection of the cells was followed by removal of the inoculum and replenishing with
950 2% FBS containing fresh media. For virus titration, aliquots of supernatant were harvested at
951 indicated time points from infected monolayers and used to infect Vero-E6 cells for foci-
952 quantification. At four days post-infection, infected Huh7 monolayers were either stained with
953 Hoechst and imaged by Olympus IX73 epi-fluorescent microscope using a 10X objective or
954 collected directly in Trizol or 4x Laemmli buffer for inactivation and downstream RNA/protein
955 quantifications. Inactivation procedures described here follow the approved standard operating
956 procedures. Equal volume of Laemmli lysates were loaded on SDS-PAGE gel for western blot
957 analysis. Equal amount of total RNA in each sample was used for strand-specific RT-qPCR.
958 Fluorescent image acquired using Blue/Green Excitation for the GFP signal and Ultraviolet
959 Excitation for the Hoechst stained nucleus. Images from the same field of view but different
960 channels were merge using ImageJ/FIJI.

961 **Strand-specific RT-qPCR**

962 Total RNA was extracted from each Trizol-inactivated sample (per well) using Direct-zol RNA
963 Miniprep Plus according to the manufacturer's protocol, eluted in 50 µl DEPC-treated water and
964 quantified by nanodrop. 200 ng of total RNA from each sample was used as the template for reverse
965 transcription (RT) using High-Capacity cDNA Reverse Transcription Kit according to the
966 manufacturer's protocol. Strand-specific RT primers were used to amplify vRNA/genome. Total
967 mRNAs, including EBOV mRNAs, were amplified using an Oligo-dT primer due to the presence of
968 poly-A tail. The resulting cDNAs were 1:100 diluted in DEPC-treated water and used in the
969 subsequent quantitative real-time PCR on a Bio-Rad CFX Real-Time System. SYBR select master
970 mix was used to mix with diluted cDNA template and target specific qPCR primer pairs in a 20 µl
971 reaction. Each reaction was performed in triplicated wells. PCR condition was following the
972 Standard Cycling Mode (Primer Tm ≥ 60 ºC) according to manufacturer's protocol. A default
973 dissociation curve was performed immediately after the real-time PCR run to obtain the Tm (melting
974 temperature) of each target. All qPCR primers specifically target EBOV sequence were confirmed
975 by detecting no signal in MOCK infected control sample. The Tm of samples using the same qPCR
976 primer pairs were confirmed are the same. Amplification plots have baseline subtracted, and the
977 relative quantification ($\Delta\Delta C_T$) method was used to analyze results. GAPDH was used as the house-
978 keeping gene for data normalization. In Figure 6B, 6G and 6H, samples from NSC were used as
979 control to calculate the relative fold-change of the target amplicon in GSPT1-knockdown

980 (GSPT1si8) samples. In Figure 6E, samples from MOCK infected cells were used as control to
981 calculate the relative fold-change of the target amplicon in EBOV infected cells.

982